REVISION 1

Crystallographic orientation relationships in host–inclusion systems: new insights from large EBSD datasets

Griffiths, Thomas A.[1*] (th.griffiths@univie.ac.at)**, Habler, Gerlinde**[1] (gerlinde.habler@univie.ac.at) **& Abart, Rainer**[1] (rainer.abart@univie.ac.at)

[1]Department of Lithospheric Research, Center for Earth Sciences, University of Vienna, Althanstrasse 14, 1090 Vienna, Austria.

[*]corresponding author

Abstract

Crystallographic orientation relationships (CORs) between mineral inclusions and their hosts could potentially deliver information about inclusion formation processes and conditions. Most previous studies are based on small numbers of analyses. This paper uses EBSD to study host–inclusion CORs in an inclusion-rich Permian metapegmatite garnet (Koralpe region, Eastern Alps, Austria), demonstrating the importance of large datasets and of EBSD in particular for the analysis of CORs. The distribution of measured orientations reflects host garnet point group symmetry for 89% of inclusions analyzed (total N = 530). Each inclusion phase (rutile, corundum and ilmenite) shows at least three different CORs to host garnet. 'Statistical' CORs are introduced to describe distributions of inclusion orientations that have one or two degrees of freedom with respect to the host, but still reflect host crystal symmetry. Two end member characteristics of statistical CORs are distinguished: rotation and dispersion. Most statistical CORs observed show a mixture of both. Each inclusion phase shows at least one statistical COR. Multiple coexisting CORs and statistical CORs are not restricted to rutile. Re-examination of previous garnet–rutile COR studies in light of the new results indicates that COR information may have been overlooked when using small datasets. Variation in COR parameters correlates with broad differences in assumed metamorphic conditions for new and literature samples, suggesting that petrogenetic information may be available if COR formation can be understood. The favorability of the detected CORs cannot be explained by a simple model involving minimization of misfit between lattice planes, implying that other interface properties or the inclusion formation mechanism are important controls on COR development.

Introduction

Crystalline mineral inclusions can provide valuable information about the formation and evolution of rocks. The origins of inclusions determine the processes about which they can record petrological information and how this information is encoded, assuming changes in the properties of interest due to re-equilibration can be excluded. In some cases, just determining the origin of a population of inclusions can have important implications for the inferred tectonometamorphic history of a sample (e.g. Green II et al. 1997; Van Roermund et al. 2000; Ye et al. 2000; Mposkos and Kostopoulos 2001; Zhang and Liou 2003; Zhang et al. 2011; Ague and Eckert Jr. 2012; Ruiz-Cruz and Sanz de Galdeano 2013; Gou et al. 2014; Glassley et al. 2014).

Many approaches to inferring inclusion origins have been taken. All studies cited in this introduction consider the phases present, their compositions, distributions, shapes and any shape-preferred orientations. Some studies also include inclusion-based microstructures (Burton 1986; Perchuk 2008; Hwang et al. 2011, 2013, 2015), compositional zoning or diffusion profiles in inclusions or hosts (Burton 1986; Ague and Eckert Jr. 2012; Hwang et al. 2013; Khisina et al. 2013), and crystallographic orientation relationships (CORs) between inclusion and host crystallographic directions (Brearley and Champness 1986; Hwang et al. 2007, 2011, 2013, 2015; Zhang et al. 2011; Proyer et al. 2013, Xu et al. 2015).

CORs have mostly been used to try to confirm exsolution origins for inclusions, due to the assumption that ‘specific’ CORs (where the crystallographic orientation of one phase is fixed relative to another) are a diagnostic criterion for exsolution (e.g. Hwang et al. 2007). However, there is a lack of agreement about criteria to distinguish between host–inclusion CORs of different origins. Combined with other observations, different specific CORs have been considered evidence both for (Hwang et al. 2011; Zhang et al. 2011) and against (Hwang et al. 2011, 2013, 2015) exsolution origins, and other authors have argued absence of a specific COR does not rule out inclusion formation by exsolution (Brearley and Champness 1986; Ague and Eckert Jr. 2012; Proyer et al. 2013; Xu et al. 2015).

Identification of inclusion origins in a sample via CORs is based on two assumptions:

1) The dataset obtained gives a representative picture of the distribution of inclusion crystallographic orientations. The CORs defined from this distribution (and the relative frequencies thereof) accurately represent the likelihood of finding an inclusion with a given crystallographic orientation relative to the host.
2) The number, relative frequencies and characteristics of CORs developed during different inclusion formation processes are known and distinguishable.

Assumption 2) requires that assumption 1) was fulfilled for any samples used to develop this knowledge, thus assumption 1) is fundamental to the determination of inclusion origins. However, many studies use only a few tens of inclusion orientations per sample to conclude which - or whether - CORs are present.

The ability of electron backscatter diffraction (EBSD) to rapidly acquire large numbers of crystallographic orientations has been exploited to obtain crystallographic orientations of rutile, corundum and ilmenite inclusions (total N = 530) in two metapegmatite garnet host grains. Using the new dataset this paper addresses the problem of how to accurately and representatively characterize the distribution of inclusion crystallographic orientations using CORs. It then discusses the potential of well-characterized sets of CORs to reveal the origins of inclusions, answer wider petrogenetic questions and shed light on the lattice-scale mechanisms controlling COR development.

Geological setting

The new dataset originates from metapegmatite garnets from the locality Wirtbartl, in the Koralpe region, Austria (sample number: 04T26K, geographic coordinates: 5177709 N, 504737 E; UTM zone 33N, geodetic datum: WGS84). The Wirtbartl metapegmatites are intercalated with metapelitic rocks of the Austroalpine Saualpe-Koralpe crystalline basement complex (Schmid et al. 2004). The complex consists mainly of poly-metamorphic siliciclastic metasediments with minor amphibolites, eclogites and metapegmatites, as well as rare calc-silicates and marbles.

The dominant tectono-metamorphic imprint in the Gneiss Unit of the Saualpe-Koralpe complex occurred at eclogite facies conditions in the Cretaceous at around 90 Ma (Thöni 2006). Maximum P-T conditions recorded by eclogites are 600 – 750ºC and 1.8 – 2.4 GPa (Gregurek et al. 1997; Miller and Thöni 1997; Miller et al. 2005, 2007). Similar temperatures but lower pressures are recorded by the metapelites (Gregurek et al. 1997; Tenczer and Stüwe 2003).

The Cretaceous tectono-metamorphic event was preceded by Permian low-pressure metamorphism, evident from garnet cores (Thöni and Miller 2009), relict assemblages (Habler and Thöni 2001; Tenczer et al. 2006) and radiometric dating (Thöni and Jagoutz 1992; Thöni et al. 2008). Permian metamorphic conditions in the Saualpe-Koralpe complex have been estimated at 600ºC/0.4 GPa (Habler and Thöni 2001) and 650ºC/0.6 – 0.65 GPa (Tenczer et al. 2006). Widespread Al-rich pegmatites give undisturbed garnet Sm–Nd ages ranging from 285 to 225 Ma, indicating multiple melt injections (Thöni et al. 2008; Thöni and Miller 2009). Pegmatites are interpreted as a product of local melting of siliciclastic (meta)sedimentary protoliths (Thöni and Miller 2000; Habler et al. 2007; Thöni et al. 2008) during long term thinning of the crust (Schuster and Stüwe 2008).

The Wirtbartl locality consists predominantly of Al-rich metapelites intercalated with peraluminous metapegmatites (Habler et al. 2007; Bestmann et al. 2008; Thöni et al. 2008). Garnet separates from different pegmatite bodies at the locality give Sm-Nd ages ranging from ca. 255 Ma (Habler et al. 2007) to ca. 230 Ma (Thöni et al. 2008).

Methods

Thin section preparation

Thin sections were polished mechanically and then chemo-mechanically (the latter using an alkaline colloidal silica suspension and a polyurethane plate) in order to produce a defect-free surface for EBSD analysis. Thin sections were carbon-coated to establish electrical conductivity. A single carbon thread at high vacuum ensured a thin coat for optimal EBSD measurement.

Field emission gun scanning electron microscope (FEG-SEM) and energy dispersive X-ray spectroscopy (EDX) analyses

Secondary electron (SE) and backscattered electron (BSE) images as well as EDX and EBSD analyses were collected on an FEI Quanta 3D FEG-SEM with a field emission gun source at the laboratory for scanning electron microscopy and focused ion beam applications of the Faculty of Geosciences, Geography and Astronomy at the University of Vienna (Austria). The microscope is equipped with an Apollo XV Silicon Drift Detector for EDX analysis. EDX data were collected using the TEAM 3.1 software at beam conditions of 15 kV and spot sizes of 4.5 - 5.5

(0.1 - 0.3 nA) in standard mode (30 - 50 µm aperture) or spot size 1.0 (4 nA) in analytic mode (1000 µm aperture).

EBSD analyses

Full crystallographic orientations of host garnet and rutile, ilmenite and corundum inclusions were determined by EBSD in two separate garnet grains. Measurements were carried out using the previously described FEI Quanta 3D FEG-SEM, equipped with an EDAX Digiview IV EBSD camera at an elevation angle of 5º. The OIM DC v6.2.1 EBSD analysis software was used for data acquisition. Beam conditions for all EBSD data were 15 kV accelerating voltage and 4.0 nA beam current with a 1000 µm SEM aperture and an incidence angle of 20º to the sample surface. The working distance was 14 mm and EBSD camera binning was 2 x 2, with Hough settings of 1º theta step size and a binned pattern size of 140 pixels. A 9 x 9 convolution mask with a maximum of 16 bands was used for indexing garnet. An 11 x 11 convolution mask with a maximum of 20 bands was used for indexing rutile, ilmenite and corundum. The same background was used throughout, but camera exposure time was increased when measuring corundum to compensate for lower signal intensity. The identity of inclusions was confirmed by EDX after measurement unless identification by EBSD pattern and inclusion habit was unequivocal. The Matlab™ toolbox MTEX (Bachmann et al. 2010; Hielscher et al. 2010) was used for data processing and pole figure plotting.

Microstructural observations

Thin section description

The original (Permian) pegmatite microstructure of the samples has been affected by Cretaceous deformation and recrystallization (Bestmann et al. 2008; Griffiths et al., 2014). Polycrystalline quartz ribbons (grain size 40 µm – 1 mm), recrystallized feldspar (K-feldspar and albite, grain size 40 – 150 μm) and acicular kyanite (grain size ~5 μm x 10 – 100 μm) define a mylonitic foliation. Magmatic almandine-spessartine garnet (grain size ~ 0.2 – 1 cm) and K-feldspar (perthitic, grain size up to ~ 1 cm) occur as porphyroclasts. Tourmaline, apatite and zircon are found as accessory minerals in the rock matrix. In less strained samples polycrystalline kyanite forms pseudomorphs completely replacing coarse-grained magmatic andalusite crystals.

In plane polarized transmitted light micrographs of thin sections garnet exhibits brownish-grey cores showing concentric and sector zoning (fig. 1), surrounded by clear pinkish rims with euhedral outer facets (fig. 2b+f). Rim garnet is intergrown with anhedral quartz (grain size 50 – 500 μm) and rare euhedral zircon (grain size ca. 100 μm). Both cores and rims are of Permian age (Thöni et al. 2008). The source of the dark coloration in cores is abundant submicrometer-sized inclusions (fig. 2), which are scarce or absent in the rims. Griffiths et al. (2014) document that these inclusions are 1 μm – 2 nm in diameter and that there are seven phases present: rutile, ilmenite, corundum, xenotime, zircon, apatite and qingheiite-Fe^{2+} (Hatert et al. 2010), a wyllieite group Fe-Mn phosphate (Moore and Ito 1979).

Inclusions define both concentric and sector zones in the garnet cores (fig. 1). Different zones are defined by variation in the abundances, grain sizes, habits or colors of the different inclusion phases. Transitions between concentric zones can be abrupt or gradual, and sometimes zoning is oscillatory (fig. 1a). Lateral transitions between sectors are always abrupt (e.g. fig. 1b). The outer boundaries of sector zones and all concentric zones are parallel to garnet crystal faces, primarily {112} and {110}.

Almost all inclusions that can be resolved optically are equant or slightly oblate, with no shape preferred orientation (fig. 2). The only exception is the intermittently developed outermost zone, which consists of elongate (0.2 – 0.5 x 10 – 100 μm) rutile needles with their long axes oriented parallel to garnet <111> directions (not shown). Corundum inclusions are almost invisible in transmitted light micrographs as they have a similar refractive index to garnet. SEM images (fig. 2d+h) reveal that they are tabular with a large aspect ratio (0.1 – 0.5 x 1 – 10 μm). Inclusions large enough to be resolved in the SEM exhibit crystal facets; apatite and wyllieite group phosphates have many facets, thus appearing rounded. Occasional multiphase inclusions can be observed.

During Cretaceous eclogite facies metamorphism garnet underwent both crystal plastic and brittle deformation. These processes locally promoted microstructural and compositional re-equilibration of inclusions and garnet, resulting in two microstructures crosscutting the inclusion zoning: recrystallization zones (Bestmann et al. 2008) and inclusion trails (Griffiths et al. 2014). Both microstructures are surrounded by garnet where sub-micrometer inclusions are absent.

EBSD measurement domains

To study possible CORs between inclusions and garnet two domains were selected (fig. 2), situated in the cores of separate but adjacent pegmatite garnets. Both have similar distributions of inclusions, though inclusions in domain A are smaller and more abundant than inclusions in domain B (fig. 2). SEM imaging and EDX measurements show that the most abundant phases in both domains are rutile, corundum and wyllieite group phosphate. No ilmenite could be detected in domain A, but ilmenite is present in domain B, where it is rarer and smaller than rutile and corundum. These differences reflect the fact that the domains are at different positions in the zoning succession. Domains were selected to avoid the areas of optically visible re-equilibration associated with inclusion trails and recrystallization zones.

Crystallographic orientation data

EBSD point analyses determined the crystallographic orientation of host garnet, corundum, rutile and ilmenite. Indexing of xenotime and zircon EBSD patterns generated multiple orientation solutions for single inclusion crystals. No reference pattern was available for wyllieite group phosphates and both wyllieite and apatite inclusions were sensitive to beam damage. In light of these methodological obstacles and their relative scarcity in the selected domains, EBSD data was not collected for zircon or any phosphate phases.

Representativeness and precision of the EBSD single point dataset

Emphasis was placed on collecting a large number of measurements for each inclusion phase; the total number of inclusions analyzed does not reflect the relative abundance of each phase. However, the relative frequency of different CORs within each phase is expected to be representative for the grainsizes that could be measured (minimum ca. 400 nm parallel to the long axis of the EBSD interaction volume) because the only selection criterion was sufficient pattern quality for indexing. All rutile and corundum CORs with N>3 inclusions were found in both garnets. Some CORs are up 2.5 times more frequent in one garnet domain compared to the other (table S1).

A rough estimate of the precision of orientation determination was obtained by calculating the average misorientation angle between five garnet orientations measured on the same crystal and the mean orientation of the five measurements. The measurements differed from the mean orientation by an average of 0.7º, and a similar value was obtained for three repeat measurements on a second garnet crystal. The estimated precision in misorientation angle between two independent measurements is thus 1.4º.

Pole figure plot construction

All pole figures were plotted with antipodal symmetry. To enable comparison between garnets all inclusion orientations were plotted relative to a fixed host garnet orientation (x ‖ $[100]_{garnet}$ and z ‖ $[001]_{garnet}$). No garnet direction was strongly preferred over any of its symmetrical equivalents for any COR in either garnet. This allowed the combination of data from separate garnets and meant that a partial symmetrization of the dataset could be carried out to make CORs clearer in pole figures without introducing spurious symmetries. Four copies of the dataset were overlapped, each rotated by 90º around garnet [001] relative to each other, forcing the dataset to conform to the fourfold symmetry of the garnet [001] axis. A single quadrant of the resulting pole figure contains the orientation relationship information of the whole dataset, combining inclusions that have CORs with symmetrically equivalent garnet axes. Symmetrized plots are indicated in figure captions.

Rutile crystallographic orientations

The crystallographic orientation of rutile inclusions relative to the host garnet reflects the symmetry of the garnet structure (fig. 3). Rutile inclusions were divided into groups based on the alignment of their <001> directions (*c*-axes) with different directions in garnet (fig. 3). Groups were divided into subgroups according to the relationships of other rutile directions with garnet. The suggested CORs of undivided rutile inclusion groups and the most abundant subgroups are listed in table 1.

Group R1 (fig. 4a). This group comprises rutile inclusions with their *c*-axes parallel to garnet <110> with ≤ 5º misorientation, corresponding to maxima in the *c*-axis ODF plot (fig. 3). Only 30% of inclusions in group R1 have *c*-axes that lie within 1.4º of garnet <110>. The distribution of misorientation angles between rutile *c*-axes and garnet <110> is shown in figure 4b. Subgroup R1a comprises the majority of group R1. One of the two symmetrically equivalent rutile *a*-axes is parallel to a garnet <111> direction and the second is parallel to a garnet <112> direction (both with up to 5º misorientation, fig. 4a). In the small subgroup R1b (fig. S1a), *a*-axes appear to follow one set of higher-order symmetrically equivalent directions in garnet. Given the 5º orientation spread it is difficult to specify these, but the garnet <144> and <118> directions are a good approximation.

Group R2 (fig. S1b). This group comprises the four rutile inclusions with a *c*-axis parallel to garnet <111> with ≤ 5º misorientation. The mean misorientation angle between rutile *c*-axes and garnet <111> is 0.7º. In subgroup R2a one of the rutile *a*-axes is parallel to a garnet <110> direction and the second is parallel to a garnet <112> direction, with no significant misorientation. The *a*-axes of one inclusion lie within a garnet {111} plane but not parallel to any low-indexed garnet directions, it is assigned to subgroup R2b.

Group R3 (fig. 5). This group comprises rutile inclusions with a *c*-axis lying in a cone inclined to the garnet <111> directions. The angle which the rutile *c*-axis makes to the nearest garnet <111> direction will be referred to as the 'inclination angle'. This relationship was previously described by Proyer et al. (2013), who recorded inclination angles from 26º - 29º (mean 27.6º). Group R3 encompasses all rutile inclusions with inclination angles of 26º - 31º (mean 28.1º). Rutile *c*-axes are not evenly distributed around garnet <111>. Six maxima form three pairs flanking each garnet <110> direction, conforming to the threefold symmetry axis along garnet <111> (fig. 3). These diffuse maxima coincide with garnet <135> directions. Three weaker maxima occur between these pairs, centered on garnet <113> directions. Group R3 was divided into 3 subgroups.

Subgroup R3a (fig. 5a), the largest, corresponds to the orientation relationship seen by Proyer et al. One rutile *a*-axis lies in or near to the {111} plane perpendicular to the <111> direction

(DOI will not work until issue is live.) DOI: http://dx.doi.org/10.2138/am-2016-5442

around which the rutile *c*-axis cone lies (fig. 5ai). The second *a*-axis is forced by symmetry to lie on a small circle at ± the inclination angle from the {111} plane, i.e. rutile orientations are tilted around the *a*-axis in the garnet {111} plane by the inclination angle. The *a*-axes in garnet {111} planes never occur within ca. 10º of a garnet <110> direction but otherwise no direction within the plane is avoided. The inclined *a*-axes show a preference for garnet <112> directions. The low-indexed rutile direction aligned closest to garnet <111> is one of the rutile <103> directions (fig. 5aii). 56% of inclusions in subgroup R3a have a rutile <103> direction within 1.4º of garnet <111>. No low-indexed garnet directions coincide with other rutile <103> directions, which lie in two cones ca. 38º and 55º inclined to garnet <111>. One small circle of {101} poles is inclined only 5º to garnet <111> and a second small circle lies at the *c*-axis inclination angle from the {111} plane, coinciding with the rutile *a*-axis small circle (fig. S2a). Rutile {101} poles show no preference for a garnet direction. All other orientation relationships described by Proyer et al. follow by symmetry from the relationships described here.

Subgroup R3b (fig. 5b) comprises group R3 inclusions where one rutile {101} plane pole is parallel to a garnet <110> direction (fig. 5bii). The *c*-axes of these inclusions cluster near to garnet <113> directions (within the previously defined cone around garnet <111>), but do not follow the <113> directions strictly. In contrast to subgroup R3a, rutile *a*-axes are not perpendicular to the garnet <111> direction around which the *c*-axis cone is located (fig. 5bi). One *a*-axis appears concentrated near to garnet <112> directions that do not lie perpendicular to garnet <111> and some rutile <103> directions seem to cluster near garnet <135> directions (fig. S2b), but there are not enough data to be confident about these potential relationships.

Subgroup R3c (fig. S2c) comprises the nine group R3 inclusions with *c*-axes that lie within the cone around a garnet <111> direction, but for which no other relationships with garnet could be found. Rutile *c*-axes cluster near to garnet <135> directions (though this was not the criteria used to define the subgroup). It is possible that there are other alignments between garnet and rutile directions but sampling statistics for this subgroup are too poor to make them obvious.

Group R1* (fig. 4c). This group represents a broad spread of *c*-axis orientations. Of all inclusions not belonging to groups R1, R2 or R3, over 80% are oriented with their *c*-axes between 5° and 22° from a garnet <110> direction (fig. 3), and are assigned to this group. The distribution of misorientation angles between rutile *c*-axes and garnet <110> is shown in figure 4b. Inclusions satisfying the *c*-axis criterion for group R3 have been excluded from group R1*. The orientation relationships of rutile directions other than <001> with garnet are as diffuse as the *c*-axis distribution. One of the two rutile *a*-axes tends to cluster parallel or near to a garnet <111> direction. However, almost no rutile *a*-axes are found aligned with a garnet <112> direction, and the remaining *a*-axes define a broad girdle around the {110} plane.

Group RX (fig S3a). This group comprises rutile inclusions where no orientation relationship with the garnet could be observed.

Corundum crystallographic orientations

The crystallographic orientation of corundum inclusions relative to the host garnet also reflects the symmetry of the garnet. Multiple groups can be identified based on the alignment of corundum <0001> directions (*c*-axes) with different garnet directions. Groups were divided into subgroups according to the relationships of other corundum directions with garnet. The CORs of undivided corundum inclusion groups and the most abundant subgroups are listed in table 2. The tabular habit of corundum inclusions is defined by their crystallography, with tablets parallel to

This is a preprint, the final version is subject to change, of the American Mineralogist (MSA)
Cite as Authors (Year) Title. American Mineralogist, in press.
(DOI will not work until issue is live.) DOI: http://dx.doi.org/10.2138/am-2016-5442

corundum {0001} planes. All corundum CORs therefore imply corresponding shape-preferred orientation relationships.

Group C1 (fig. 6a). This group comprises corundum inclusions with a *c*-axis parallel to the garnet <112> direction with ≤ 5º misorientation. 78% of these inclusions have a *c*-axis within 1.4º of garnet <112>. Most inclusions belong to subgroup C1a. One corundum *a*-axis (parallel to the poles of corundum {11-20} planes) is aligned with a garnet <111> direction (fig 6ai). By symmetry the other two *a*-axes align close to garnet <113> directions. Correspondingly, corundum {10-10} poles are aligned at 30º to the *a*-axes, one {10-10} pole is fixed parallel to garnet <110> and the other two lie near to garnet <135> directions (fig 6aii). The small subgroup C1b is identical to C1a except that inclusions are rotated 30º around their *c*-axes. Two inclusions have *a*-axes in garnet {112} planes that are not parallel to any of the important garnet directions seen in the other subgroups, these are assigned to subgroup C1c.

Group C2 (fig. 6b). This group comprises corundum inclusions with a *c*-axis parallel to the garnet <111> direction with ≤ 5º misorientation. 84% of the group has a *c*-axis within 1.4º of garnet <111>. Almost all inclusions are assigned to subgroup C2a, where all corundum *a*-axes (fig 6bi) are parallel to garnet <112> directions and all {10-10} poles (fig. 6bii) are parallel to garnet <110> directions. Subgroup C2b comprises the 3 inclusions where corundum *a*-axes are merely located within a garnet {111} plane and are not systematically parallel to a low-indexed garnet direction.

Group C3 (fig. S4). This group comprises the small number of corundum inclusions with a *c*-axis parallel to the garnet <100> direction with ≤ 5º misorientation. The mean misorientation angle between group C3 corundum *c*-axes and garnet <100> is 1.47º. One corundum *a*-axis is always parallel to a garnet <110> direction, as by symmetry is one {10-10} pole.

Group C4 (fig. 6c). This group comprises corundum inclusions without a *c*-axis within ≤ 5º misorientation angle of either garnet <111> or <112> directions, but with one *a*-axis (fig. 6ci) parallel to a garnet <111> direction (with ≤ 5º misorientation). 38% of inclusions in the group have one *a*-axis within 1.4º of garnet <111>. The corundum *c*-axes lie in {111} garnet planes, as does one of the {10-10} poles (fig. 6cii). This group has not been divided into subgroups as there are no symmetrically repeated concentrations of corundum {10-10} poles, *c*- or *a*-axes parallel to low indexed garnet directions. Nonetheless group C4 corundum *c*-axes do not appear randomly distributed around one *a*-axis, but this may be an artifact of the small number of grains comprising this group.

Group CX (fig S3b). This group comprises corundum inclusions where no orientation relationship with the garnet could be observed.

Ilmenite crystallographic orientations

The crystallographic orientation of ilmenite inclusions relative to the host garnet also reflects garnet symmetry. Groups were defined based on the alignment of ilmenite <0001> directions (*c*-axes) with different garnet directions and divided into subgroups using the relationships of other ilmenite directions with garnet. The CORs of undivided ilmenite inclusion groups and the most abundant subgroups are listed in table 3.

Group I1 (fig. 7a). This group comprises ilmenite inclusions with a *c*-axis parallel to the garnet <112> direction with ≤ 5º misorientation. 86% of the group has their *c*-axis within 1.4º of garnet <112>. In the largest subgroup, I1a, one ilmenite *a*-axis (equivalent to one ilmenite {11-20} plane pole) is aligned with a garnet <111> direction (fig. 7ai). The other *a*-axes align close to garnet <113> directions. One ilmenite {10-10} pole is fixed parallel to garnet <110> and the other two lie near to garnet <135> directions (fig. 7aii). The small subgroup I1b is identical to I1a except that inclusions are rotated 30º around their *c*-axes. Six inclusions have *a*-axes in garnet {112} planes that are not parallel to any of the important garnet directions seen in the other subgroups, these are assigned to subgroup I1c.

Group I2 (fig. 7b). This group comprises ilmenite inclusions with a *c*-axis parallel to the garnet <111> direction with ≤ 5º misorientation. 95% of the group has a *c*-axis within 1.4º of garnet <111>. All but one inclusion are assigned to subgroup I2a, where all ilmenite *a*-axes are parallel to garnet <112> directions (fig. 7bi) and all {10-10} poles are parallel to garnet <110> directions (fig. 7bii). A single inclusion has *a*-axes located within a garnet {111} plane but not parallel to a low-indexed garnet direction, assigned to subgroup I2b.

Group I3 (fig. 7c). This group comprises ilmenite inclusions without a *c*-axis within ≤ 5º misorientation angle of either garnet <111> or <112> directions, but with one *a*-axis (fig. 7ci) parallel to a garnet <111> direction (with ≤ 5º misorientation). 65% of inclusions in the group have one *a*-axis within 1.4º of garnet <111>. The ilmenite *c*-axes lie in {111} garnet planes, as does one of the {10-10} poles (fig. 7cii). This group has not been divided into subgroups as there are no symmetrically repeated concentrations of ilmenite {10-10} poles, *c*- or *a*-axes parallel to low indexed garnet directions.

Group IX (fig S3c). This group comprises ilmenite inclusions where no orientation relationship with the garnet could be observed.

Discussion

89% of the 530 inclusions analyzed by EBSD have crystallographic orientations that can be related to the crystal symmetry of the host garnet. Each of the three inclusion phases examined can be divided among at least three different groups (most with several subgroups) on the basis of orientation relationships between host and inclusion crystallographic directions. The Wirtbartl host–inclusion system displays exceptional variety in the number and type of CORs present.

The origin of the Wirtbartl inclusions is not discussed here. This would require a full picture of the CORs present in host–inclusion systems with different known inclusion origins, something this paper suggests is not yet available.

Types of COR

Nomenclature is required to discuss the diverse characteristics of the observed CORs. The proposed terminology for COR types does not carry any genetic implications. In this discussion, the term 'specific COR' refers to a crystallographic orientation relationship where the orientations of inclusion and host are fixed with respect to one another, with zero degrees of freedom. It makes no reference to the coherency of the two lattices or the interface geometry and structure.

About half the COR groups described do not show a specific COR to the host garnet. Nonetheless, the distribution of inclusion crystallographic orientations in these groups reflects the symmetry of the garnet (e.g. fig. 3). The term 'statistical COR' is introduced to describe the relationships between host and inclusion directions that are not specific but non-random. A statistical COR is defined by a population of inclusions. The crystallographic orientations of individual inclusions with a particular statistical COR have one or more degrees of freedom relative to the crystallographic orientation of the host, although there may be limits to the range of misorientation angles over which this freedom exists. EBSD measurement of increasing numbers of inclusions with the same statistical COR reveals an orientation distribution that increasingly accurately approximates conformity to the centrosymmetric point group symmetry of the host crystal.

The inclusion orientation distributions of statistical CORs display two end member characteristics. A statistical COR usually exhibits a mixture of both. In some groups, one inclusion crystallographic direction is fixed to the host and the others are free to assume any direction rotated around this common axis, i.e. inclusion crystallographic orientations have one degree of freedom (subgroup R3a, fig. 5a; group C4, fig. 6c; subgroup I1c, fig. 7a; group I3, fig. 7c; Proyer et al. 2013; Xu et al. 2015). This characteristic of a statistical COR will be referred to as 'rotation'. 'Rotational' statistical CORs are those where rotation is the strongest element of the inclusion orientation distribution. In most examples the single degree of freedom is limited, so that not every orientation distributed around a certain direction is equally favored (e.g. subgroup R3a, fig. 5a; Xu et al. 2015).

Other groups show inclusion crystallographic directions concentrated within a certain misorientation angle of particular host crystallographic directions, but not fixed exactly parallel to them (groups R1 and R1*, fig. 4; subgroups R3b and R3c, figs. 5b & S2c). Such groups allow two degrees of freedom between host and inclusion crystallographic orientations, but only within strict limits. This characteristic of a statistical COR will be referred to as 'dispersion'. 'Dispersional' statistical CORs are those where dispersion is the strongest element of the inclusion orientation distribution; if one crystallographic direction were less dispersed then the statistical COR would be rotational in character. Rotational CORs often show subordinate dispersion (all rotational CORs listed in the previous paragraph; Xu et al. 2015).

Due to the complexity inherent in precisely determining the error of lattice orientations derived from SEM-EBSD analyses (e.g. Ram et al. 2015), a generalized criterion to differentiate specific CORs from statistical CORs at very small dispersions is beyond the scope of this paper. In the Wirtbartl dataset the two predominantly dispersional statistical CORs (groups R1 and R1*) can nonetheless be reliably classified because the observed dispersion greatly exceeds the expected angular error of Hough-transform-based EBSD (fig. 4).

An indication of the amount of dispersion of an axis relationship can be obtained by calculating the fraction of inclusions in a group that fulfill the chosen relationship with a misorientation angle below a set value. This has been carried out for the Wirtbartl dataset for groups containing > 10 inclusions, using an angle of 1.4°, twice the approximate angular precision of the garnet orientation measurements. For axis relationships that are considered specific (groups C1, C2, I1 and I2) > 75% of all inclusions have misorientation angles of less than 1.4°, whereas in groups with minor or major dispersional character, < 65% of all inclusions fulfill this criterion. It is not considered useful to subdivide groups depending on whether each inclusion exceeds the angular cutoff or not as there is no evidence that there would be a physical or genetic distinction between the resulting subgroups.

Table S2 summarizes how the CORs of all (sub)groups listed in tables 1 – 3 have been classified, according to the criteria discussed above.

Why use the statistical COR concept?

General considerations. Currently, studies of host–inclusion systems often look for evidence of specific CORs, rather than fully describing the distribution of inclusion orientations present. The statistical COR concept encourages a less binary approach, in accordance with the wide variety of CORs observed in this and other studies (Proyer et al. 2013; Xu et al. 2015) that are not specific. It also highlights the need for larger numbers of orientation measurements when studying CORs.

Once inclusion directions are separated by less than twice the angular error of the EBSD measurement from each other, the distribution of directions is indistinguishable from continuous. Below this limit (e.g. subgroup R3a, fig. 5a; group C4, fig. 6c) it is inappropriate to represent the distribution of orientations as a large number of different specific CORs.

Illustrative case study: re-examination of Hwang et al. (2007, 2015). Re-examining some previous results provides an example of how the concept of statistical CORs can capture details of host–inclusion crystallographic relationships that are otherwise obscured.

Hwang et al. (2015) present TEM data on the interfaces and CORs of rutile needles in garnet from multiple sources: detrital Idaho 'star garnet' most likely originally from polymetamorphic amphibolite facies metapelitic schist (West et al. 2005; Lang et al. 2014) and garnets from two ultra-high-pressure (UHP) localities: an eclogite from the Sulu UHP terrane in China and a microdiamond-bearing rock from the Erzgebirge, Germany. The Idaho garnets are the main focus of the study, whereas the UHP sample measurements are an expansion of a smaller dataset presented in Hwang et al. (2007).

Hwang et al. (2015) define seven major garnet–rutile CORs, all exclusively specific. Their COR-1, COR-5 and COR-6 are not found in the Wirtbartl garnets, and their COR-4 (corresponding to subgroup R2a) is present but rare in both datasets. Comparison of the three remaining Hwang et al. CORs with the rotational statistical COR of group R3a provides evidence of statistical CORs in the older datasets. Rutile inclusions with crystallographic orientations corresponding to

Hwang et al.'s COR-2 & COR-2' ($[103]_{Rt} \parallel [111]_{Grt}$ & $(0\pm10)_{Rt} \parallel (4\text{-}3\text{-}1)_{Grt}$, COR-2 and COR-2' are indistinguishable by EBSD) are common in the Wirtbartl garnets. The same is true for their COR-3 ($[103]_{Rt} \parallel [111]_{Grt}$ & $(010)_{Rt} \parallel (2\text{-}1\text{-}1)_{Grt}$). For the Wirtbartl dataset it is immediately obvious that the <010> directions (*a*-axes) of inclusions with $<103>_{Rt} \parallel <111>_{Grt}$ are not *limited* to being parallel to either $<4\text{-}3\text{-}1>_{Grt}$ or $<2\text{-}1\text{-}1>_{Grt}$. Rutile *a*-axes can lie anywhere in the {111} plane, with the exception of positions within ca. 10º of a garnet <110> direction (group R3a, fig. 5ai).

Hwang et al. (2015) document rutile inclusions with small misorientations from their specific CORs, describing these as 'angular misfits of xº' or 'xº off' from a particular axis relationship. Multiple angular misfits are explicitly described in the Hwang et al. (2015) measurements from the Sulu UHP garnet sample. For inclusions close to COR-2/2', the reported range of angular misfits is greater (0 - 6º) for rutile *a*-axes than for the perpendicular rutile <103> directions (0 - 2º), i.e. these inclusions are misoriented around a rotation axis close to garnet <111> from the ideal COR. Inclusions close to COR-3 reportedly do not show any angular misfit for rutile <103> directions but show angular misfits of 0 - 3º for their *a*-axes, corresponding to a pure rotation around garnet <111>. Taking the extremes of both ranges implies that only 7º of the 16.1º angle between neighboring $<2\text{-}1\text{-}1>_{Grt}$ and $<4\text{-}3\text{-}1>_{Grt}$ directions remains unoccupied by rutile *a*-axes in the reported dataset. Given that the Sulu garnet dataset presented in Hwang et al. (2015) consists of only 19 rutile inclusion orientations, 17 with COR-2/2' or COR-3 orientations, there is a strong possibility that further measurements might reveal a continuous distribution of rutile *a*-axes in the garnet {111} plane, similar to that of the Wirtbartl garnets. This possibility is supported by the 5 Sulu rutile needles plotted by Hwang et al. (2007) that have *c*-axes in a cone around a garnet <111> direction and *a*-axes in a garnet {111} plane (implying one $<103>_{Rt}$ is approximately parallel to $\langle 111\rangle_{Grt}$). None of these inclusions have *a*-axes that coincide with $\langle 2\text{-}1\text{-}1\rangle_{Grt}$, $\langle 4\text{-}3\text{-}1\rangle_{Grt}$, or $\langle 1\text{-}10\rangle_{Grt}$, and one particular *a*-axis (a_6) is approximately halfway between a $\langle 2\text{-}1\text{-}1\rangle_{Grt}$ and a $\langle 4\text{-}3\text{-}1\rangle_{Grt}$ direction (fig. 8).

Hwang et al. (2015) do not explicitly give the percentage of inclusions with angular misfits for every sample, but in contrast to the Sulu garnets, the Idaho star garnets appear to mostly show inclusions without angular misfits. Of 58 inclusions measured in one sample (a 6-ray star garnet showing 6 different CORs), only one is called out as having any angular misfit. The distribution of rutile inclusion crystallographic orientations in the 6-ray Idaho star garnet is therefore best described by multiple specific CORs, even using the stricter definition preferred in this paper.

The existence of a range of rutile inclusion crystallographic orientations arrayed around a common host garnet axis (a rotational statistical COR) is a reproducible and important characteristic of the Sulu garnet samples that is obscured by describing the distribution as a number of specific CORs with ‘angular misfit[s]’. The Sulu orientation distribution appears distinguishable from that in the Idaho star garnets, where the large majority of rutile inclusions *do* have completely specific CORs (assuming that all instances of angular misfit have been explicitly reported). This fact may be of petrological significance, but previous terminology has not allowed for such distinctions to be unambiguously stated.

A final judgment on the continuity of rutile *a*-axis distributions in garnet {111} planes in the Sulu samples must await measurement of a larger number of rutile crystallographic orientations. However, even if further measurements were to confirm the current angular misfit ranges for COR-2/2’ and COR-3 as the maximum variation present in the Sulu sample, the description of these CORs as specific would remain misleading. If the current ranges describe the true maximum variation, the individual groupings COR-2, COR-2' and COR-3 can be retained. However, they should then be described as rotational statistical CORs to denote the nature of the angular variation within each population. Should further measurements instead reveal a continuous distribution, a single rotational statistical COR would most correctly describe the systematic distribution of inclusion orientations with $\langle 103 \rangle_{Rt} \parallel \langle 111 \rangle_{Grt}$.

The uncertainty about the rotational statistical COR(s) in the Sulu sample stems directly from the limited number of rutile crystallographic orientations reported so far. However, no matter how large the dataset, small groups of inclusions from which the full particulars of a COR cannot be reliably determined will almost always be found (e.g. subgroup R2b, fig. S1b; subgroups C1c & C2b, fig. 6a+b; subgroups I1c & I2b, fig. 7a+b). The most general description for a group of inclusions with one axis fixed relative to the host is a single rotational statistical COR, and in the absence of sufficient measurements to reveal greater detail, this is the recommended description. The inclusions in the Sulu sample with $\langle 103 \rangle_{Rt} \parallel \langle 111 \rangle_{Grt}$ should be described as belonging to a single rotational statistical COR until further data becomes available.

Comparison of Wirtbartl COR data with literature CORs

Existing literature data on CORs between garnet and corundum are restricted to intergrowths between corundum and yttrium aluminium garnet. Sugiyama et al. (2009) found the same COR as the commonest COR in this study (subgroup C1a, fig. 6a), $\langle 0001 \rangle_{corundum\ (Crn)} \parallel \langle 112 \rangle_{garnet\ (Grt)}$ & $\{11\text{-}20\}_{Crn} \parallel \{111\}_{Grt}$. Frazer et al. (2001) detected the COR $\langle 0001 \rangle_{Crn} \parallel \langle 112 \rangle_{Grt}$ & $\{10\text{-}10\}_{Crn} \parallel \{111\}_{Grt}$, observed only rarely in this study (subgroup C1b, fig. 6a). No literature could be located on CORs between garnet and ilmenite. However, in the Wirtbartl data there is great similarity between the CORs of the two different trigonal phases with garnet. All COR groups identified for ilmenite are also shown by corundum. This similarity extends to broader similarity with literature data for CORs between trigonal and cubic crystals. The hematite-magnetite system shows condition-dependent variation between the axis relationships $<0001>_{\text{hematite (Hem)}}$ $\|<111>_{\text{magnetite (Mag)}}$ and $<0001>_{\text{Hem}} \|<112>_{\text{Mag}}$ (Bursill & Withers 1979), and for the axis relationship $<0001>_{\text{Hem}} \|<111>_{\text{Mag}}$ both the relationships $\{10\text{-}10\}_{\text{Hem}} \| \{110\}_{\text{Mag}}$ (e.g. Bursill & Withers 1979) and the relationship $\{11\text{-}20\}_{\text{Hem}} \| \{110\}_{\text{Mag}}$ (Amouric et al. 1986) have been found to exist. The range of possible CORs between two phases can seemingly be estimated knowing only their respective crystal systems, suggesting that the role of conserved symmetry elements in controlling CORs is large. Despite the existence of a range of *possible* CORs, the simultaneous occurrence of so many of these in one system does appear to be an unusual feature of the Wirtbartl garnets.

At present, the host–inclusion system for which the most varied COR data is available is the garnet–rutile system. Despite uncertainties concerning inclusion formation mechanisms and the conditions and timing of COR formation, an overview of reported garnet–rutile CORs gives an indication of distinguishable characteristic features and possible trends. Rutile–garnet CORs have been described from five garnet localities: detrital ‘star garnets’ most likely from polymetamorphic amphibolite facies metapelitic schists (West et al. 2005; Lang et al. 2014) in Idaho (Guinel & Norton 2006; Hwang et al. 2015); garnets from eclogite layers in an ultramafic complex in the Sulu UHP terrane, China (Hwang et. al 2007, 2015); garnets containing microdiamonds from the Erzgebirge, Germany (Hwang et. al 2007, 2015); granulite facies garnet rims on UHP garnets from a kyanite-garnet mica-schist in the Kimi complex, Rhodope Massif, Greece (Proyer et al. 2013); and low pressure pegmatite garnets from the locality Wirtbartl, Koralpe, Eastern alps (this study). The Erzgebirge garnet–rutile CORs are not described in sufficient detail to judge whether they are statistical or specific, so are not included in the discussion below.

The axis relationship $\langle 103\rangle_{\mathrm{rutile\ (Rt)}}$ ‖ $\langle 111\rangle_{\mathrm{Grt}}$ is found at every locality, but there are differences in the arrangement of rutile *a*-axes in {111} garnet planes between the localities. In Idaho star garnet there are reportedly multiple specific CORs involving $\langle 103\rangle_{\mathrm{Rt}}$ ‖ $\langle 111\rangle_{\mathrm{Grt}}$, with COR-2/2' rutile *a*-axes parallel to $\langle 4\text{-}3\text{-}1\rangle_{\mathrm{Grt}}$ (the sole COR present in one garnet analyzed), COR-3 rutile *a*-axes parallel to $\langle 2\text{-}1\text{-}1\rangle_{\mathrm{Grt}}$ and COR-1 rutile *a*-axes parallel to $\langle 1\text{-}10\rangle_{\mathrm{Grt}}$ (Hwang et al. 2015). This last axis relationship is found *only* in the Idaho garnets. In contrast, there is a single rotational statistical COR around $\langle 103\rangle_{\mathrm{Rt}}$ ‖ $\langle 111\rangle_{\mathrm{Grt}}$ reported for rutile needles in garnet from the Rhodope and from equant rutile inclusions in this study (subgroup R3a), with rutile *a*-axes found at all points in the garnet {111} plane apart from close to garnet $\langle 1\text{-}10\rangle$ directions (this study fig. 5; Proyer et al. 2013). The dataset is of limited size, but the same rotational statistical COR also seems to be shared by inclusions with $\langle 103\rangle_{\mathrm{Rt}}$ ‖ $\langle 111\rangle_{\mathrm{Grt}}$ in the Sulu garnets (Hwang et al. 2007, 2015). Rutile inclusions with *c*-axes concentrated on dispersional statistical CORs around garnet $\langle 110\rangle$ directions comprise ca. 50% of the 250 inclusions measured in the Wirtbartl samples, but are not observed at any of the other localities. The COR $\langle 001\rangle_{\mathrm{Rt}}$ ‖ $\langle 111\rangle_{\mathrm{Grt}}$ & $\langle 010\rangle_{\mathrm{Rt}}$ ‖ $\langle 1\text{-}10\rangle_{\mathrm{Grt}}$ is found in the Idaho garnets (where it is designated COR-4), the Rhodope garnets, and in this study (corresponding to subgroup R2a), but is very rare in all cases. CORs involving $\langle 001\rangle_{\mathrm{Rt}}$ ‖ $\langle 001\rangle_{\mathrm{Grt}}$ are found occasionally in the Sulu garnets and commonly in certain Idaho garnets (11 of 58 inclusions measured in one garnet have Hwang et al.'s COR-5; $[001]_{\mathrm{Rt}}$ ‖ $[001]_{\mathrm{Grt}}$ & $(010)_{\mathrm{Rt}}$ ‖ $(1\text{-}10)_{\mathrm{Grt}}$), such CORs are not found elsewhere.

The data available show that multiple rutile–garnet CORs are common in single localities and that similarities exist between CORs over a wide range of conditions. This suggests strong favorability of certain axis relationships. Whether this is a consequence of energetically favorable lattice-scale interactions or common inclusion formation processes (or both) is unknown. Alongside broad similarities there are variations between (and in the case of the Idaho garnets even within) localities. The two localities with at least one unique COR (Idaho and Wirtbartl) are the two with very different implied conditions of formation to the UHP and granulite garnets. The Wirtbartl data are the only results from equant rutile inclusions rather than needles, this may also contribute to the observed differences. The literature comparison corroborates the impression given by the corundum and ilmenite data that the Wirtbartl garnets exhibit an unusually high number of different CORs for a single locality.

Lattice-based explanations for the Wirtbartl CORs?

A lattice matching (or coherency) model (e.g. Howe 1997; Balluffi et al. 2005) predicts orientation relationships well for phases with similar crystal symmetries and structures. However, the Wirtbartl inclusions have heterophase interfaces, separating different crystal systems and oxygen sublattices. Calculated lattice strain was used to compare parallel sets of planes from observed CORs to examine whether lattice matching can explain their favorability. Physically, lattice mismatches may be accommodated by elastic strain, misfit dislocations or an incoherent interface (Howe 1997).

Tables 1 – 3 list the sets of parallel garnet and inclusion plane poles or directions that define the largest COR (sub)groups. Whenever directions are listed, the indices of the direction are identical to the pole of a plane with equivalent indices. A pair of parallel related planes was designated *(hkl)* for garnet and *(mno)* for inclusions. The d-spacings of sets of garnet planes (*HKL*) = *x**(*hkl*) and inclusion planes *(MNO)* = *y**(*mno*) were used to calculate lattice strains. The variables *x* and *y* are positive scalar integers. Calculated lattice strains depend on the size of *x* and *y*, referred to here as the 'order' of the *(HKL)* and *(MNO)* planes. In this work low-order planes are preferred, as these are more likely to correspond to layers of atoms in the crystal. The lowest-order pair of planes that could achieve a strain of between -0.04 and +0.04 (an arbitrary target) was determined for each planar relationship in tables 1 – 3. Lattice strain was calculated as $\frac{d_{(MNO)\ inclusion} - d_{(HKL)\ garnet}}{d_{(HKL)\ garnet}}$, where $d_{(MNO)}$ represents the d-spacing of *(MNO)* planes. If only very high order planes met the target, the strain for a 1:*x* or *y*:1 ratio of orders was calculated for comparison purposes, with *x* (or *y*) chosen to minimize the lattice strain. The results are given in tables 4 – 6. Bolded relationships are those where the target lattice strain can be achieved using orders ≤ 3, assumed to indicate the best matches.

Using $d_{\text{inclusion}}$ as the denominator instead has negligible effect for small lattice strains. For lattice strains > 0.1 there is a difference of ≥ 20%. The effect of pressure has been neglected as the pegmatites formed at no more than 0.3 GPa (Habler et al. 2007). Calculations used lattice constants measured at room pressure and at room temperature and 600ºC (table S3). Room temperature values are discussed here; lattice strains calculated using cell parameters at 600ºC differ by ≤ 0.01 (tables S4-S6).

The lattice-matching hypothesis posits that common, specific CORs should have multiple good d-spacing fits between inclusion and host, with rotational CORs occurring where one set of planes has a much better fit than the planes oriented at a high angle to them.

Rutile CORs (table 4). A good low-indexed fit was not found for the relationship $\{001\}_{\text{rutile (Rt)}} \parallel \{110\}_{\text{garnet (Grt)}}$, which fits with the observation that although rutile *c*-axes are concentrated near garnet <110> directions there is significant dispersion (subgroup R1a, group R1*, fig. 4). The calculated fits for the rutile {100} plane relationships of subgroup R1a are good, including a 1:1 correspondence between $\{100\}_{\text{Rt}}$ and $\{112\}_{\text{Grt}}$ with only 3% misfit. Despite this, rutile *a*-axes show similar amounts of dispersion to the *c*-axes for subgroup R1a, and the relationship $\{100\}_{\text{Rt}} \parallel \{112\}_{\text{Grt}}$ is absent in group R1*.

Only one of the three sets of planes examined for each COR in subgroups R2a and R3b shows a good calculated fit with garnet. Despite this, neither COR shows a rotational component, although both are rare as would be expected for poorly fitting CORs.

In subgroup R3a a single rutile <103> direction (pole to a {405} rutile plane) is aligned (sub)parallel to garnet <111>. There is a poor fit between rutile {405} planes and garnet, the most plausible relationship being $\{405\}_{\text{Rt}} \parallel \{12\ 12\ 12\}_{\text{Grt}}$ (lattice strain 0.06). However, the <103> rutile vector is almost exactly equal to half the <111> garnet vector (misfit strain only 0.004). Despite poor agreement between {405} rutile planes and garnet plane families parallel to {111}, the similarity between crystal vector lengths somehow favors this axial orientation relationship. Rutile inclusions can rotate around the fixed <103> direction despite the good fits exhibited by rutile {100} planes.

Corundum CORs (table 5). Despite only one set of planes having a low-indexed, low lattice strain fit with garnet, subgroup C1a is specific and also the commonest corundum COR. Subgroup C2a is slightly less common than subgroup C1a, despite being the *only* COR for which three perpendicular sets of well-fitting planar relationships are calculated. No good low index fit exists for the only fixed set of planes of the group C4 rotational statistical COR. No rotational statistical COR is developed around the much better fitting pair of $\{10\text{-}10\}_{corundum} \parallel \{220\}_{Grt}$ planes (lattice strain -0.01).

Ilmenite CORs (table 6). Ilmenite subgroups I1a and I2a share the same COR as corundum subgroups C1a and C2a. But whereas in subgroup C1a the {10-10} planes achieve the lowest lattice strains with garnet, in subgroup I1a the best fits were achieved by planes parallel to {0001}. This does fit with the greater number of inclusions rotated around their *c*-axes for ilmenite as compared to corundum (compare subgroup C1c, 1% of all corundum orientations, with subgroup I1c, 7% of all ilmenite orientations).

In group I3, the only good alignment is $\{33\text{-}60\}_{Ilm} \parallel \{888\}_{Grt}$ (lattice strain -0.01). The fact that these are the only fixed planes of a rotational statistical COR may suggest that this high-indexed planar relationship is actually favorable.

Evaluation. The calculated lattice strains and plane indices are not very effective at explaining the CORs observed. Although at least one set of low-indexed inclusion planes usually fits well with garnet for each group/subgroup, the results do not reflect the observed relative frequencies of each COR and cannot explain why a particular COR is specific or statistical. An interface-scale factor not addressed here is the nature of bonding across the host–inclusion interface. Strong (and thus energetically favorable) bonds between atoms preferentially exposed at certain orientations of interface planes could encourage specific relationships that appear unfavorable due to lattice strain alone.

It appears that the continuation of symmetry elements between host and inclusion has a strong influence on CORs. Many CORs with only a single set of well-fitting planes are nonetheless specific rather than rotational statistical, and the same direction (the {11-20} pole) is the axis of a rotational statistical COR for both trigonal phases, despite the fact that for corundum in particular, other planes would theoretically have better fits. One possible factor which could favor continuation of symmetry elements is the minimization of elastic strain energy between host and inclusion at a larger scale than individual lattice planes, controlling CORs by the interaction of host and inclusion elastic properties. These do have several characteristics similar to statistical CORs. The {111} planes in garnet, populated by rutile *a*-axes of the subgroup R3a rotational statistical COR, are planes of constant garnet stiffness. Regions of shallow gradients in elastic properties exist around low-indexed garnet crystallographic directions, coinciding with axis relationships where dispersion of rutile directions is seen. This explanation has difficulty explaining the importance of the rutile <103> direction however, as this is a direction of neither minimum nor maximum stiffness in rutile, and the resulting conical distribution of the stiff (relative to garnet) rutile *c*-axis does not follow contours of constant garnet stiffness.

Implications

This work shows that multiple coexisting CORs and statistical CORs between host and inclusions are not an isolated quirk of rutile inclusions in garnet. Studies based on relatively small numbers of inclusion orientations have likely overlooked statistical CORs and underestimated the true variety of CORs present, with implications for interpretations of inclusion origins.

It is essential to test the above hypothesis and discover how widespread the features of CORs identified in the Wirtbartl garnets are. Future studies of host–inclusion systems should involve large numbers of measurements in order to accommodate the concept of statistical CORs and obtain a representative picture of the frequency of the different CORs detected. EBSD is the optimum method to achieve COR characterization within a reasonable timeframe. Context from EBSD measurements greatly increases the value of any TEM data obtained on individual inclusions and avoids unrepresentative conclusions.

The CORs defined for a given sample should be guided by the amount of data available, the limitations of the methods employed, the aims of the study, and prior knowledge of the system. As decisions about how to describe a distribution of inclusion orientations can influence the way a dataset is presented, future studies should explicitly discuss their reasons for defining each COR reported. Failure to do this could obscure important aspects of the data.

Sufficiently large numbers of measurements of inclusion orientations provide information on many different parameters: which - and how many - CORs each inclusion phase assumes, the relative frequencies of these CORs, whether these CORs are specific or statistical, and the amount of rotation and dispersion of each statistical COR. A survey of rutile inclusion CORs in garnet from multiple localities suggests these parameters are likely affected by processes of inclusion formation / incorporation and/or variables such as pressure, temperature, cooling rate, composition, interface geometry, nucleation rate, or growth rate. An improved understanding of the small and large scale processes controlling the development of the full range of host-inclusion CORs could deliver information not only about the origins of the inclusions involved but also the conditions at the time of formation.

It is currently not possible to predict the favorability of particular CORs from knowledge of host and inclusion crystal lattices. A simple model involving the minimization of misfits between parallel sets of host and inclusion lattice planes could not fully explain the frequency or characteristics of the CORs observed in the Wirtbartl samples, implying that unaccounted for interface-scale factors (e.g. atomic bonding), long range interactions such as elastic strain and/or the formation mechanisms of the inclusions may be important factors. Combined EBSD and TEM studies of systems where the origin of inclusions is independently known are necessary to determine the influence of inclusion formation processes on the resulting CORs. Improved computer models of the 3D atomic structure of interfaces will make it possible to probe the influence of other variables on the favorability of different CORs. An ultimate goal would be to be able to divide inclusions into COR groups based on physical characteristics of their interfaces and genetic considerations.

Acknowledgements

The authors acknowledge funding by the University of Vienna doctoral school IK052 Deformation of Geological Materials (DOGMA) and the project of the Austrian Science Fund (FWF): I471-N19, as part of the international DFG-FWF funded research network FOR741-DACH. Dr. Helen M. Lang is thanked for providing information about the presumed source rocks of the Idaho star garnets.

References

Ague, J.J., and Eckert Jr., J.O. (2012) Precipitation of rutile and ilmenite needles in garnet: Implications for extreme metamorphic conditions in the Acadian Orogen, U.S.A. American Mineralogist, 97, 840–855.

Amouric, M., Baronnet, A., Nahon, D., and Didier, P. (1986) Electron microscopic investigations of iron oxyhydroxides and accompanying phases in lateritic iron-crust pisolites. Clays and Clay Minerals, 34, 45–52.

Bachmann, F., Hielscher, R., and Schaeben, H. (2010) Texture analysis with MTEX- Free and open source software toolbox. Solid State Phenomena, 160, 63–68.

Balluffi, R.W., Allen, S., and Carter, W.C. (2005) Kinetics of Materials, 674 p. John Wiley & Sons, Hoboken.

Bestmann, M., Habler, G., Heidelbach, F., and Thoni, M. (2008) Dynamic recrystallization of garnet and related diffusion processes. Journal of Structural Geology, 30, 777–790.

Brearley, A.J., and Champness, P.E. (1986) Magnetite exsolution in almandine garnet. Mineralogical Magazine, 50, 621–633.

Bursill, L.A., and Withers, R.L. (1979) On the multiple orientation relationships between hematite and magnetite. Journal of Applied Crystallography, 12, 287–294.

Burton, K.W. (1986) Garnet-quartz intergrowths in graphitic pelites: the role of the fluid phase. Mineralogical Magazine, 50, 611–620.

Frazer, C.S., Dickey, E.C., and Sayir, A. (2001) Crystallographic texture and orientation variants in Al2O3-Y3Al5O12 directionally solidified eutectic crystals. Journal of Crystal Growth, 233, 187–195.

Glassley, W.E., Korstgård, J.A., Ensen, K.S., and Platou, S.W. (2014) A new UHP metamorphic complex in the ~1.8 Ga Nagssugtoqidian Orogen of west Greenland. American Mineralogist, 99, 1315–1334.

Gou, L., Zhang, C., Zhang, L., and Wang, Q. (2014) Precipitation of rutile needles in garnet from sillimanite-bearing pelitic granulite from the Khondalite Belt, North China Craton. Chinese Science Bulletin, 59, 4359–4366.

Green II, H.W., Dobrzhinetskaya, L., Riggs, E.M., and Jin, Z.-M. (1997) Alpe Arami: A peridotite massif from the mantle transition zone? Tectonophysics, 279, 1–21.

Gregurek, D., Abart, R., and Hoinkes, G. (1997) Contrasting Eoalpine P-T evolutions in the southern Koralpe, Eastern Alps. Mineralogy and Petrology, 60, 61–80.

Griffiths, T.A., Habler, G., Rhede, D., Wirth, R., Ram, F., and Abart, R. (2014) Localization of submicron inclusion re-equilibration at healed fractures in host garnet. Contributions to Mineralogy and Petrology, 168, 1–21.

Guinel, M.J.-F., and Norton, M.G. (2006) The origin of asterism in almandine-pyrope garnets from Idaho. Journal of Materials Science, 41, 719–725.

Habler, G., and Thöni, M. (2001) Preservation of Permo–Triassic low-pressure assemblages in the Cretaceous high-pressure metamorphic Saualpe crystalline basement (Eastern Alps, Austria). Journal of Metamorphic Geology, 19, 679–697.

Habler, G., Thöni, M., and Miller, C. (2007) Major and trace element chemistry and Sm-Nd age correlation of magmatic pegmatite garnet overprinted by eclogite-facies metamorphism. Chemical Geology, 241, 4–22.

Hatert, F., Baijot, M., Philippo, S., and Wouters, J. (2010) Qingheiite-(Fe2+), Na2Fe2+MgAl(PO4)3, a new phosphate mineral from the Sebastião Cristino pegmatite, Minas Gerais, Brazil. European Journal of Mineralogy, 22, 459–467.

Hielscher, R., Schaeben, H., and Siemes, H. (2010) Orientation distribution within a single hematite crystal. Mathematical Geosciences, 42, 359–375.

Howe, J.M. (1997) Interfaces in Materials: Atomic Structure, Thermodynamics and Kinetics of Solid-Vapor, Solid-Liquid and Solid-Solid Interfaces. John Wiley & Sons, Hoboken.

Hwang, S.L., Yui, T.F., Chu, H.T., Shen, P., Schertl, H.P., Zhang, R.Y., and Liou, J.G. (2007) On the origin of oriented rutile needles in garnet from UHP eclogites. Journal of Metamorphic Geology, 25, 349–362.

Hwang, S.-L., Yui, T.-F., Chu, H.-T., Shen, P., Zhang, R.-Y., and Liou, J.G. (2011) An AEM study of garnet clinopyroxenite from the Sulu ultrahigh-pressure terrane: formation mechanisms of oriented ilmenite, spinel, magnetite, amphibole and garnet inclusions in clinopyroxene. Contributions to Mineralogy and Petrology, 161, 901–920.

Hwang, S.L., Shen, P., Chu, H.T., Yui, T.F., and Iizuka, Y. (2013) A TEM study of the oriented orthopyroxene and forsterite inclusions in garnet from Otrøy garnet peridotite, WGR, Norway: new insights on crystallographic characteristics and growth energetics of exsolved pyroxene in relict majoritic garnet. Journal of Metamorphic Geology, 31, 113–130.

Hwang, S.-L., Shen, P., Chu, H.-T., Yui, T.-F., and Iizuka, Y. (2015) Origin of rutile needles in star garnet and implications for interpretation of inclusion textures in ultrahigh-pressure metamorphic rocks. Journal of Metamorphic Geology, 33, 249–272.

Lang, H.M., Johnson, S.E., and Largent, K.J. (2014) Use of garnet zoning and pseudosection modeling to constrain the P-T path of metapelitic tectonites in the snow peak area, northern Idaho. Geological Society of America Abstracts with Programs, 46, 140.

Miller, C., and Thöni, M. (1997) Eo-Alpine eclogitisation of Permian MORB-type gabbros in the Koralpe (Eastern Alps, Austria): New geochronological, geochemical and petrological data. Chemical Geology, 137, 283–310.

Miller, C., Thöni, M., Konzett, J., Kurz, W., and Schuster, R. (2005) Eclogites from the Koralpe and Saualpe type-localities, eastern Alps, Austria. Mitteilungen der Österreichischen Mineralogischen Gesellschaft, 227–263.

Miller, C., Zanetti, A., Thöni, M., and Konzett, J. (2007) Eclogitisation of gabbroic rocks: Redistribution of trace elements and Zr in rutile thermometry in an Eo-Alpine subduction zone (Eastern Alps). Chemical Geology, 239, 96–123.

Moore, P., and lto, J. (1979) Alluaudites, wyllieites, arrojadites: crystal chemistry and nomenclature. Mineralogical Magazine, 43, 227–235.

Mposkos, E.D., and Kostopoulos, D.K. (2001) Diamond, former coesite and supersilicic garnet in metasedimentary rocks from the Greek Rhodope: a new ultrahigh-pressure metamorphic province established. Earth and Planetary Science Letters, 192, 497–506.

Proyer, A., Habler, G., Abart, R., Wirth, R., Krenn, K., and Hoinkes, G. (2013) TiO2 exsolution from garnet by open-system precipitation: evidence from crystallographic and shape preferred orientation of rutile inclusions. Contributions to Mineralogy and Petrology, 166, 211–234.

Ram, F., Zaefferer, S., Jäpel, T., and Raabe, D. (2015) Error analysis of the crystal orientations and disorientations obtained by the classical electron backscatter diffraction technique. Journal of Applied Crystallography, 48.

Ruiz-Cruz, M.D., and Sanz de Galdeano, C. (2013) Coesite and diamond inclusions, exsolution microstructures and chemical patterns in ultrahigh pressure garnet from Ceuta (Northern Rif, Spain). Lithos, 177, 184–206.

Schmid, S.M., Fügenschuh, B., Kissling, E., and Schuster, R. (2004) Tectonic map and overall architecture of the Alpine orogen. Eclogae Geologicae Helvetiae, 97, 93–117.

Schuster, R., and Stüwe, K. (2008) Permian metamorphic event in the Alps. Geology, 36, 603–606.

Sugiyama, K., Nakai, M., AYoshikawa, and Fukuda, T. (2009) Microstructure and crystal chemistry of eutectic Al2O 3/Y3Al5O12 Fibers Modified by the Partial Substitution of Sc2O3 for Al2O 3. High Temperature Materials and Processes, 28, 89–95.

Tenczer, V., and Stüwe, K. (2003) The metamorphic field gradient in the eclogite type locality, Koralpe region, Eastern Alps. Journal of Metamorphic Geology, 21, 377–393.

Tenczer, V., Powell, R., and Stüwe, K. (2006) Evolution of H2O content in a polymetamorphic terrane: the Plattengneiss Shear Zone (Koralpe, Austria). Journal of Metamorphic Geology, 24, 281–295.

Thöni, M. (2006) Dating eclogite-facies metamorphism in the Eastern Alps - Approaches, results, interpretations: A review. Mineralogy and Petrology, 88, 123–148.

Thöni, M., and Jagoutz, E. (1992) Some new aspects of dating eclogites in orogenic belts: Sm-Nd, Rb-Sr, and Pb-Pb isotopic results from the Austroalpine Saualpe and Koralpe type-locality (Carinthia/Styria, southeastern Austria). Geochimica et Cosmochimica Acta, 56, 347–368.

Thöni, M., and Miller, C. (2000) Permo-triassic pegmatites in the eo-alpine eclogite-facies Koralpe complex, Austria: Age and magma source constraints from mineral chemical, Rb-Sr and Sm-Nd isotope data. Schweizerische Mineralogische und Petrographische Mitteilungen, 80, 169–186.

——— (2009) The “Permian event” in the Eastern European Alps: Sm–Nd and P–T data recorded by multi-stage garnet from the Plankogel unit. Chemical Geology, 260, 20–36.

Thöni, M., Miller, C., Zanetti, A., Habler, G., and Goessler, W. (2008) Sm-Nd isotope systematics of high-REE accessory minerals and major phases: ID-TIMS, LA-ICP-MS and EPMA data constrain multiple Permian-Triassic pegmatite emplacement in the Koralpe, Eastern Alps. Chemical Geology, 254, 216–237.

Van Roermund, Drury, Barnhoorn, and De Ronde (2000) Super-silicic garnet microstructures from an orogenic garnet peridotite, evidence for an ultra-deep (>6 GPa) origin. Journal of Metamorphic Geology, 18, 135–147.

West, N., Foley, N., and Evans, J. (2005) Garnet gravels and their source rocks: a comparative study of garnet resources of the Emerald Creek area, Idaho. Geological Society of America Abstracts with Programs, 37, 63.

Xu, H., Zhang, J., Zong, K., and Liu, L. (2015) Quartz exsolution topotaxy in clinopyroxene from the UHP eclogite of Weihai, China. Lithos, 226, 17–30.

Ye, K., Cong, B., and Ye, D. (2000) The possible subduction of continental material to depths greater than 200 km. Nature, 407, 734–736.

Zhang, J.F., Xu, H.J., Liu, Q., Green, H.W., and Dobrzhinetskaya, L.F. (2011) Pyroxene exsolution topotaxy in majoritic garnet from 250 to 300 km depth. Journal of Metamorphic Geology, 29, 741–751.

Zhang, R.Y., and Liou, J.G. (2003) Clinopyroxenite from the Sulu ultrahigh-pressure terrane, eastern China: Origin and evolution of garnet exsolution in clinopyroxene. American Mineralogist, 88, 1591–1600.

Figure Captions

FIGURE 1. Transmitted plane polarized light micrographs of thin sections show concentric (**a**) and sector (**b**) zoning in Wirtbartl metapegmatite garnets, defined by variations in inclusion abundances, grain sizes and habits. Inclusion trails with bleaching zones (Griffiths et al. 2014) crosscut the zoning. Oscillatory zoning visible at bottom right of (**a**).

FIGURE 2. Inclusion EBSD measurement domains A (**a-d**) and B (**e-h**). Optical overviews of each domain [(**a**) and (**e**)] show the regions from which inclusion orientations were obtained (black dashed lines), the number of measurements made, and the positions of optical close-ups [(**c**) and (**g**), pink rectangles] and BSE images [(**d**) and (**h**), orange rectangles]. (**b**) and (**f**) provide optical context, the areas shown in (**a**) and (**e**) are indicated by yellow polygons.

FIGURE 3. The orientation distribution function (ODF) of all measured rutile inclusion <001> directions, plotted relative to a fixed garnet orientation (antipodal, equal angle, upper hemisphere pole figure). The halfwidth (HW) and intensity of the ODF are indicated to the right of the pole figure, and the ODF color scale is shown below. Garnet crystallographic directions are indicated by colored squares and triangles, see legend above the pole figure. Colored small circles indicate rutile *c*-axis criteria used to define the groups of rutile inclusions set out in table 1: R1 = dark grey, R1* = light blue, R3 = red. Group R2 *c*-axis maxima are hidden by overlying garnet <111> symbols.

FIGURE 4. EBSD data from rutile inclusions in groups R1 and R1* plotted relative to a fixed garnet orientation. Both plots are antipodal, equal angle, upper hemisphere pole figures. Garnet directions are indicated by colored squares and triangles, see legend in figure 3. (**a**) Orientation of rutile <001> (red) and <100> (blue) directions for group R1. Dark grey small circles have a

radius of 5°. (**b**) Histogram showing the distribution of misorientation angles (in degrees) between rutile *c*-axes and garnet <110> directions for groups R1 and R1*. Bins are 1° wide. (**c**) Orientation of rutile <001> directions for groups R1 (red) and R1* (light blue). Also plotted is an ODF of group R1* <100> directions (color scale as in fig. 3). The halfwidth (HW), minimum and maximum intensity of the ODF are indicated to the right of the pole figure. Small circles of 5° (dark grey) and 22° (light blue) are drawn around the garnet [0-11] direction. A fourfold rotation was used to combine symmetrically equivalent inclusion data into a single pole figure quadrant (see section ‘pole figure plot construction’).

FIGURE 5. EBSD data from rutile inclusions in subgroups R3a and R3b plotted relative to a fixed garnet orientation. All plots are antipodal, equal angle, upper hemisphere pole figures. Garnet directions are indicated by colored squares and triangles, see legend in figure 3. A fourfold rotation was used to combine inclusion data from symmetrically equivalent garnet directions into a single pole figure quadrant for all plots (see section ‘pole figure plot construction’). Red small circles are at inclination angles of 26° and 31° from garnet [111]. (**a**) The orientation of rutile <001> (red, **i**+**ii**), <100> (blue, **i**) and <103> (blue, **ii**) directions for subgroup R3a (legend above each figure). Black small circles are at inclination angles of 62° and 90° to garnet [111] for (**i**) and 38° and 55° to garnet [111] for (**ii**). (**b**) The orientation of rutile <001> (red, **i**+**ii**) and <100> (blue, **i**) directions and {101} (blue, **ii**) plane poles for subgroup R3b (legend above each figure). Black small circles are at inclination angles of 62° and 90° to garnet [111] for (**i**).

FIGURE 6. EBSD data from corundum inclusions in groups C1 (**a**), C2 (**b**) and C4 (**c**) plotted relative to a fixed garnet orientation. Poles to corundum {0001} planes are indicated in all plots as red circles. In addition, the left column of plots (**i**) shows corundum {11-20} plane poles

(blue) and the right column (**ii**) shows {10-10} poles (blue) for each group. All plots are antipodal, equal angle, upper hemisphere pole figures. Garnet directions are indicated by colored squares and triangles, see legend in figure 3. A fourfold rotation was used to combine inclusion data from symmetrically equivalent garnet directions into a single pole figure quadrant for all plots (see section 'pole figure plot construction'). Black small circles indicate (**a**) garnet {112} planes (**b**) a garnet {111} plane (**ci**) a garnet {111} plane and a cone inclined at 60° to garnet [111] and (**cii**) a garnet {111} plane and a cone inclined at 30° to garnet [111].

FIGURE 7. EBSD data from ilmenite inclusions in groups I1 (**a**), I2 (**b**) and I3 (**c**) plotted relative to a fixed garnet orientation. Poles to ilmenite {0001} planes are indicated in all plots as red circles. In addition, the left column of plots (**i**) shows ilmenite {11-20} plane poles (blue) and the right column (**ii**) shows {10-10} poles (blue). All plots are antipodal, equal angle, upper hemisphere pole figures. Garnet directions are indicated by colored squares and triangles, see legend in figure 3. A fourfold rotation was used to combine inclusion data from symmetrically equivalent garnet directions into a single pole figure quadrant for all plots (see section 'pole figure plot construction'). Black small circles indicate (**a**) garnet {112} planes (**b**) a garnet {111} plane (**ci**) a garnet {111} plane and a cone inclined at 60° to garnet [111] and (**cii**) a garnet {111} plane and a cone inclined at 30° to garnet [111].

FIGURE 8. Equal angle projection plot of rutile orientation data adapted from Hwang et al. (2007). The original plot is underlain by small circles at 28° and 33° to one garnet <111> direction (red continuous lines) and small circles at 57° and 90° to the same direction (blue dotted lines, dots 2° apart). Garnet <134> (orange triangles) and <112> (green triangles) directions in the (-11-1) garnet plane are plotted, and do not coincide with rutile *a*-axes a_1 or a_3 – a_6, which belong to rutile inclusions with *c*-axes (c_1 & c_3 – c_6) inclined on cones to garnet [-11-1]

(red small circles). Figure used by permission of John Wiley and Sons, from Hwang et al. (2007), Journal of Metamorphic Petrology, vol. 25, Fig. 3, p. 354.

Tables

TABLE 1. Relationships between crystallographic directions of rutile inclusions and host garnet

Group	rt *c*-axis ∥ grt <uvw>	N (gp.)	Largest subgroup(s)	(sub)group rt *a*-axis ∥ grt <uvw>	(sub)group rt {101} ∥ grt <uvw>	(sub)group rt <103> ∥ grt <uvw>	N (sgp.)
R1	grt <110> (±5°)	43	R1a	grt <111> (±5°) (1ax) grt <112> (±5°) (1ax)	-	-	39
R1*	grt <110> (>5°, <22°)	84	-	concentrated at grt <111> (1ax)	n.o.	n.o.	-
R2	grt <111>	4	R2a	grt <110> (1ax) grt <112> (1ax)	-	-	3
R3	Cone around grt <111> (28.5° ± 2.5)	103	R3a	1ax in grt {111} plane (±5°), avoid grt <110>	n.o.	grt <111> (±5°) (1ax)	80
			R3b	Never in grt {111} plane 1ax near grt <112>	grt <110> (1ax)	n.o.	14
RX	n.o.	16	-	n.o.	n.o.	n.o.	-

Notes: rt = rutile; grt = garnet; gp. = group; sgp = subgroup; n.o. = not observed. The largest subgroup in each group is detailed in this table. Additional subgroups with N ≥10 are also included. Where two orientation relationships are enough to define a specific COR, the other columns are left blank (-).The number of symmetrically equivalent crystallographic directions which follow each relationship is indicated (1ax = one direction, 2ax = 2 directions, no comment = all equivalent directions share the relationship).

TABLE 2. Relationships between crystallographic directions of corundum inclusions and host garnet

Group	crn *c*-axis ∥ grt <uvw>	N (gp.)	Largest subgroup	(sub)group crn *a*-axis ∥ grt <uvw>	(sub)group crn {10-10} pole ∥ grt <uvw>	N (sgp.)
C1	grt <112>	69	C1a	grt <111> (1ax) near grt <113> (2ax)	grt <110> (1ax) near grt <135> (2ax)	62
C2	grt <111>	56	C2a	grt <112>	grt <110>	53
C3	grt <100>	3	-	grt <110> (1ax)	grt <110> (1ax)	-
C4	in grt {111}	28	-	grt <111> (±5°)	1ax in grt {111} plane (±5°)	-
CX	n.o.	24	-	n.o.	n.o.	-

Notes: crn = corundum; grt = garnet; gp. = group; sgp = subgroup; n.o. = not observed. The largest subgroup in each group is detailed in this table. No additional subgroups with N ≥ 10 were found. The number of symmetrically equivalent crystallographic directions which follow each relationship is indicated (1ax = one direction, 2ax = 2 directions, no comment = all equivalent directions share the relationship).

TABLE 3. Relationships between crystallographic directions of ilmenite inclusions and host garnet

Group	ilm *c*-axis ‖ grt <uvw>	N (gp.)	Largest subgroup	(sub)group ilm *a*-axis ‖ grt <uvw>	(sub)group ilm {10-10} pole ‖ grt <uvw>	N (sgp.)
I1	grt <112>	28	I1a	grt <111> (1ax) near grt <113> (2ax)	grt <110> (1ax) near grt <135> (2ax)	21
I2	grt <111>	21	I2a	grt <112>	grt <110>	20
I3	in grt {111}	35	-	grt <111> (±5°)	1ax in grt {111} plane (±5°)	-
IX	n.o.	16	-	n.o.	n.o.	-

Notes: ilm = ilmenite; grt = garnet; gp. = group; sgp = subgroup; n.o. = not observed. The largest subgroup in each group is detailed in this table. No additional subgroups with N ≥ 10 were found. The number of symmetrically equivalent crystallographic directions which follow each relationship is indicated (1ax = one direction, 2ax = 2 directions, no comment = all equivalent directions share the relationship).

TABLE 4. Calculation of lattice strains for parallel sets of rutile and garnet planes determined using EBSD.

(Sub)group	CORs from EBSD (format: rt ‖ grt)	Lowest index planes ($-0.04 \le \varepsilon \le 0.04$) (format: rt ‖ grt)	ε	Best fit 1 : x d-spacing ratio (format: rt ‖ grt)	ε (1 : x d-spacing ratio)
R1a	{001} ‖ {110}	{003} ‖ {880}	0.04	{001} ‖ {330}	-0.08
	{100} ‖ {112} *(1ax)*	**{100} ‖ {112}**	**0.03**	-	-
R1a / R1*	**{100} ‖ {111} *(1ax)***	**{200} ‖ {333}**	**-0.03**	-	-
R2a	{001} ‖ {111}	{003} ‖ {777}	-0.03	{001} ‖ {222}	0.12
	{100} ‖ {112} *(1ax)*	**{100} ‖ {112}**	**0.03**	-	-
	{100} ‖ {110} *(1ax)*	{004} ‖ {777}	0.02	{100} ‖ {220}	-0.12
R3a	**<103> ‖ <111>**	**<206> ‖ <111>**	**0.00**	-	-
	{405} ‖ {111}	{405} ‖ {13 13 13}	-0.02	{405} ‖ {12 12 12}	0.06
R3b	{001} ‖ {113}	{005} ‖ {6 6 18}	-0.02	{001} ‖ {113}	0.15
	{100} ‖ {112} *(1ax)*	**{100} ‖ {112}**	**0.03**	-	-
	{101} ‖ {110}	{303} ‖ {10 10 0}	-0.01	{101} ‖ {330}	0.09

Notes: rt = rutile; grt = garnet; ε = calculated lattice strain. Lattice strains given to 2 decimal places, at this degree of precision errors in lattice constants used for the calculation are too small to affect the result. Bolded relationships are those where the target lattice strain can be achieved with a simple 1:x or 2:x d-spacing ratio. The number of symmetrically equivalent crystallographic directions which follow each relationship is indicated (1ax = one direction, no comment = all equivalent directions share the relationship).

TABLE 5. Calculation of lattice strains for parallel sets of corundum and garnet planes determined using EBSD.

(Sub)group	CORs from EBSD (format: crn ‖ grt)	Lowest index planes ($-0.04 \leq \varepsilon \leq 0.04$) (format: crn ‖ grt)	ε	Best fit 1 : x d-spacing ratio (format: crn ‖ grt)	ε (1 : x d-spacing ratio)
C1a	{0001} ‖ {112}	{0008} ‖ {336}	-0.03	{0003} ‖ {112}	0.08
	{11-20} ‖ {111} *(1ax)*	{4 4 -8 0} ‖ {11 11 11}	0.02	{11-20} ‖ {333}	-0.07
	{10-10} ‖ {110} *(1ax)*	**{10-10} ‖ {220}**	**-0.01**	-	-
C2a	**{0001} ‖ {111}**	**{0002} ‖ {111}**	**0.03**	-	-
	{11-20} ‖ {112}	**{11-20} ‖ {224}**	**-0.01**	-	-
	{10-10} ‖ {110}	**{10-10} ‖ {220}**	**-0.01**	-	-
C3	{0001} ‖ {001}	{0007} ‖ {006}	0.04	{0001} ‖ {001}	-0.12
	{11-20} ‖ {110} *(1ax)*	{22-40} ‖ {770}	-0.02	{11-20} ‖ {330}	0.13
	{10-10} ‖ {110} *(1ax)*	**{10-10} ‖ {220}**	**-0.01**	-	-
C4	{11-20} ‖ {111} *(1ax)*	{4 4 -8 0} ‖ {11 11 11}	0.02	{11-20} ‖ {333}	-0.07

Notes: crn = corundum; grt = garnet; ε = calculated lattice strain. Lattice strains given to 2 decimal places, at this degree of precision errors in lattice constants used for the calculation are too small to affect the result. Bolded relationships are those where the target lattice strain can be achieved with a simple 1:x or 2:x d-spacing ratio. The number of symmetrically equivalent crystallographic directions which follow each relationship is indicated (1ax = one direction, no comment = all equivalent directions share the relationship).

TABLE 6. Calculation of lattice strains for parallel sets of ilmenite and garnet planes determined using EBSD.

(Sub)group	CORs from EBSD (format: ilm ‖ grt)	Lowest index planes ($-0.04 \leq \varepsilon \leq 0.04$) (format: ilm ‖ grt)	ε	Best fit 1 : x d-spacing ratio (format: ilm ‖ grt)	ε (1 : x d-spacing ratio)
I1a	**{0001} ‖ {112}**	**{0003} ‖ {112}**	**0.01**	-	-
	{11-20} ‖ {111} *(1ax)*	{33-60} ‖ {888}	-0.01	{11-20} ‖ {333}	-0.14
	{10-10} ‖ {110} *(1ax)*	{50-50} ‖ {990}	-0.01	{10-10} ‖ {220}	-0.08
I2a	{0001} ‖ {111}	{0 0 0 13} ‖ {6 6 6}	0.03	{0002} ‖ {111}	-0.05
	{11-20} ‖ {112}	{5 5 -10 0} ‖ {9 9 18}	0.03	{11-20} ‖ {224}	-0.08
	{10-10} ‖ {110}	{50-50} ‖ {990}	-0.01	{10-10} ‖ {220}	-0.08
I3	{11-20} ‖ {111}	{33-60} ‖ {888}	-0.01	{11-20} ‖ {333}	-0.14

Notes: ilm = ilmenite; grt = garnet; ε = calculated lattice strain. Lattice strains given to 2 decimal places, at this degree of precision errors in lattice constants used for the calculation are too small to affect the result. Bolded relationships are those where the target lattice strain can be achieved with a simple 1:x or 2:x d-spacing ratio. The number of symmetrically equivalent crystallographic directions which follow each relationship is indicated (1ax = one direction, no comment = all equivalent directions share the relationship).

Figure 1

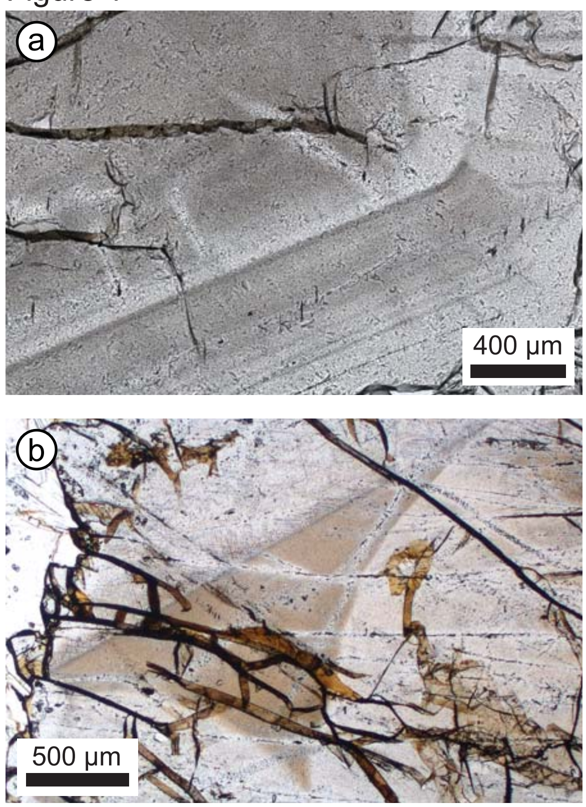

Figure 2

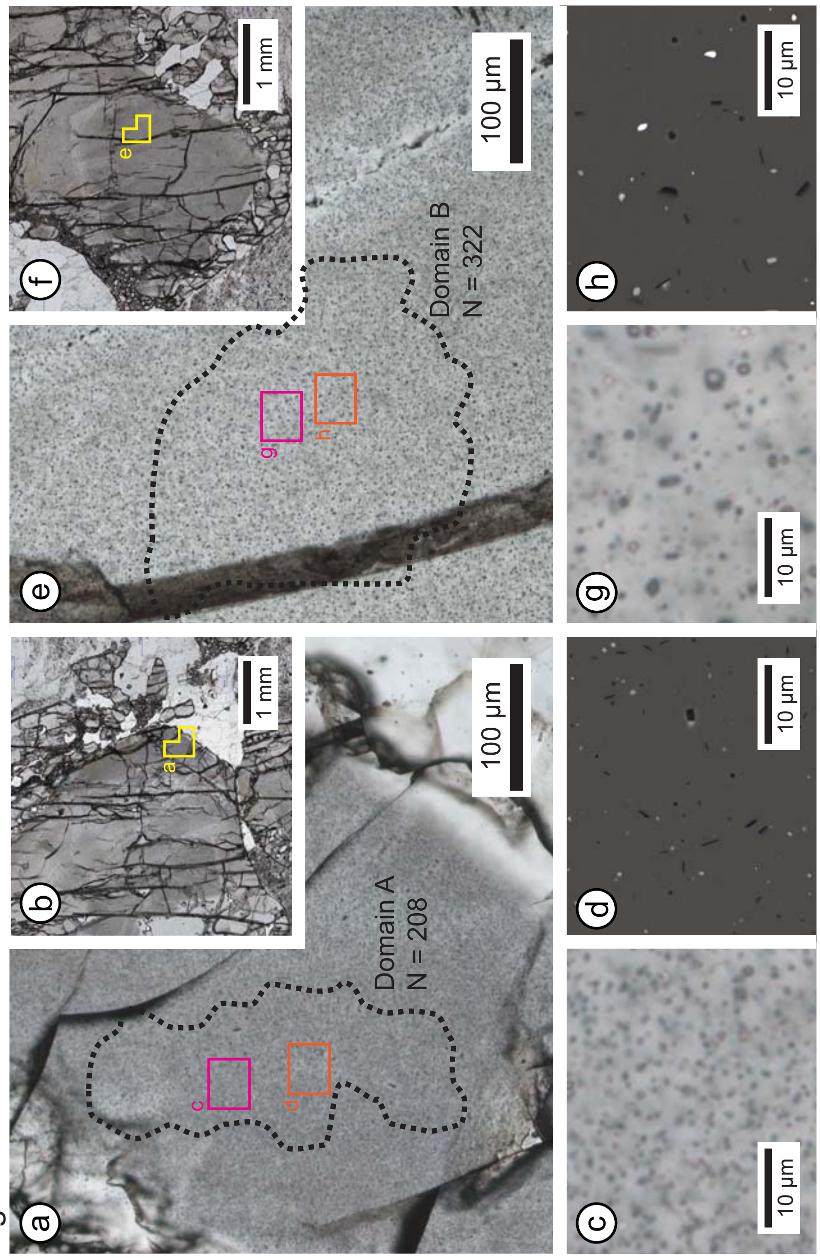
a
b
c
d
e
f
g
h
Domain A
N = 208
Domain B
N = 322
100 µm
100 µm
1 mm
1 mm
10 µm
10 µm
10 µm
10 µm

Figure 3

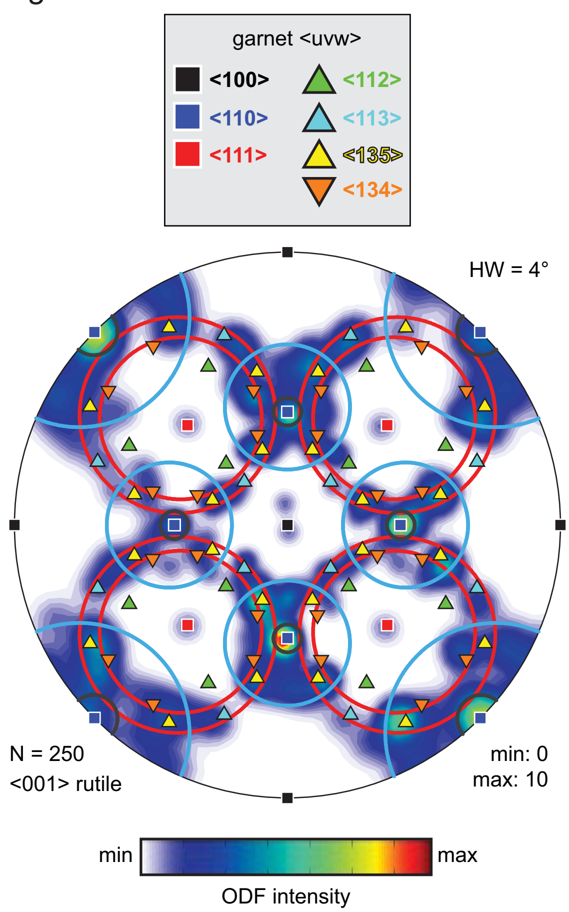
garnet <uvw>
<100>
<110>
<111>
<112>
<113>
<135>
<134>
HW = 4°
N = 250
<001> rutile
min: 0
max: 10
min
max
ODF intensity

Figure 4

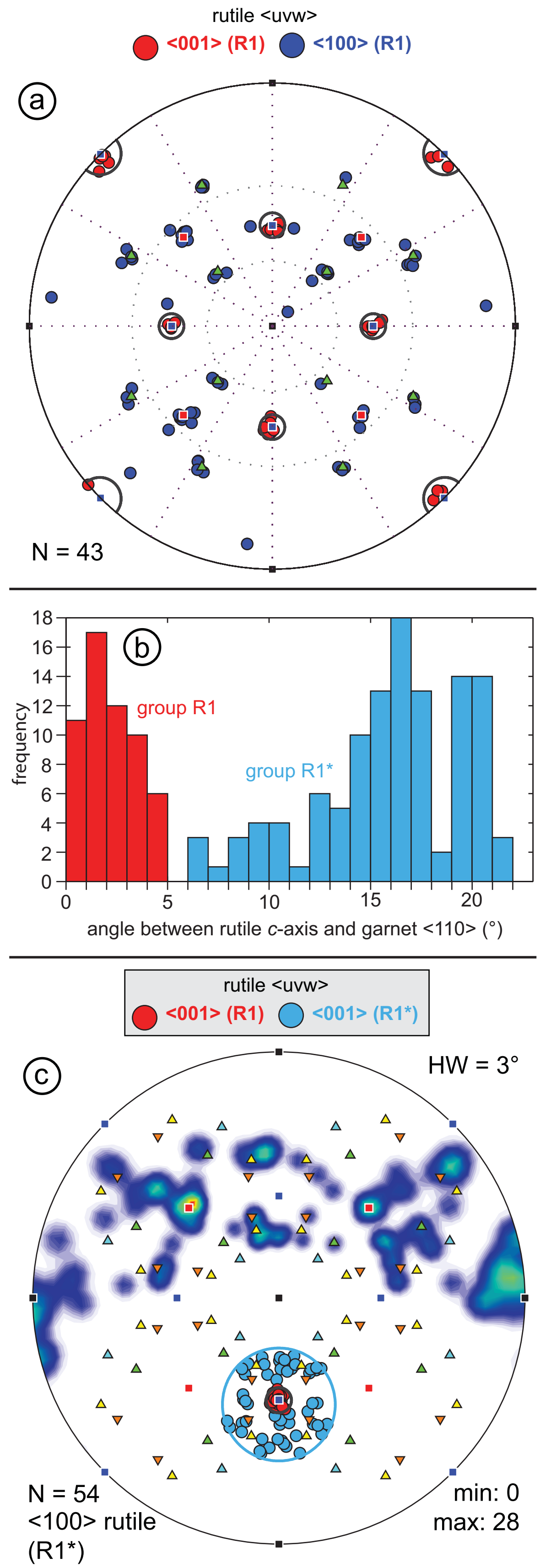
rutile <uvw>
<001> (R1)
<100> (R1)
a
N = 43
b
group R1
group R1*
frequency
angle between rutile c-axis and garnet <110> (°)
0
5
10
15
20
18
16
14
12
10
8
6
4
2
0
rutile <uvw>
<001> (R1)
<001> (R1*)
c
HW = 3°
N = 54
<100> rutile
(R1*)
min: 0
max: 28

Figure 5

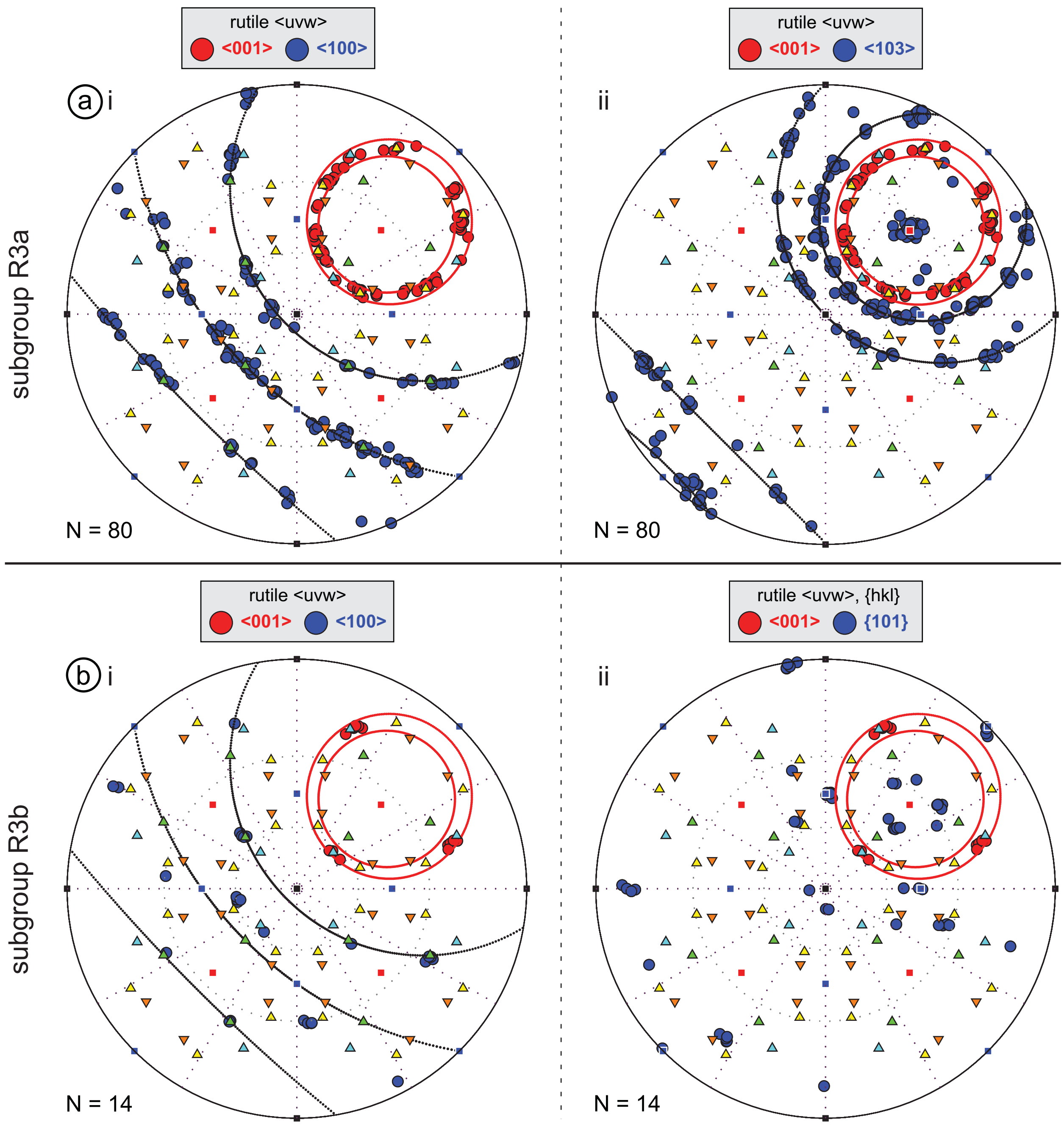
rutile <uvw>
<001> <100>
rutile <uvw>
<001> <103>
a i
ii
subgroup R3a
N = 80
N = 80
rutile <uvw>
<001> <100>
rutile <uvw>, {hkl}
<001> {101}
b i
ii
subgroup R3b
N = 14
N = 14

Figure 6

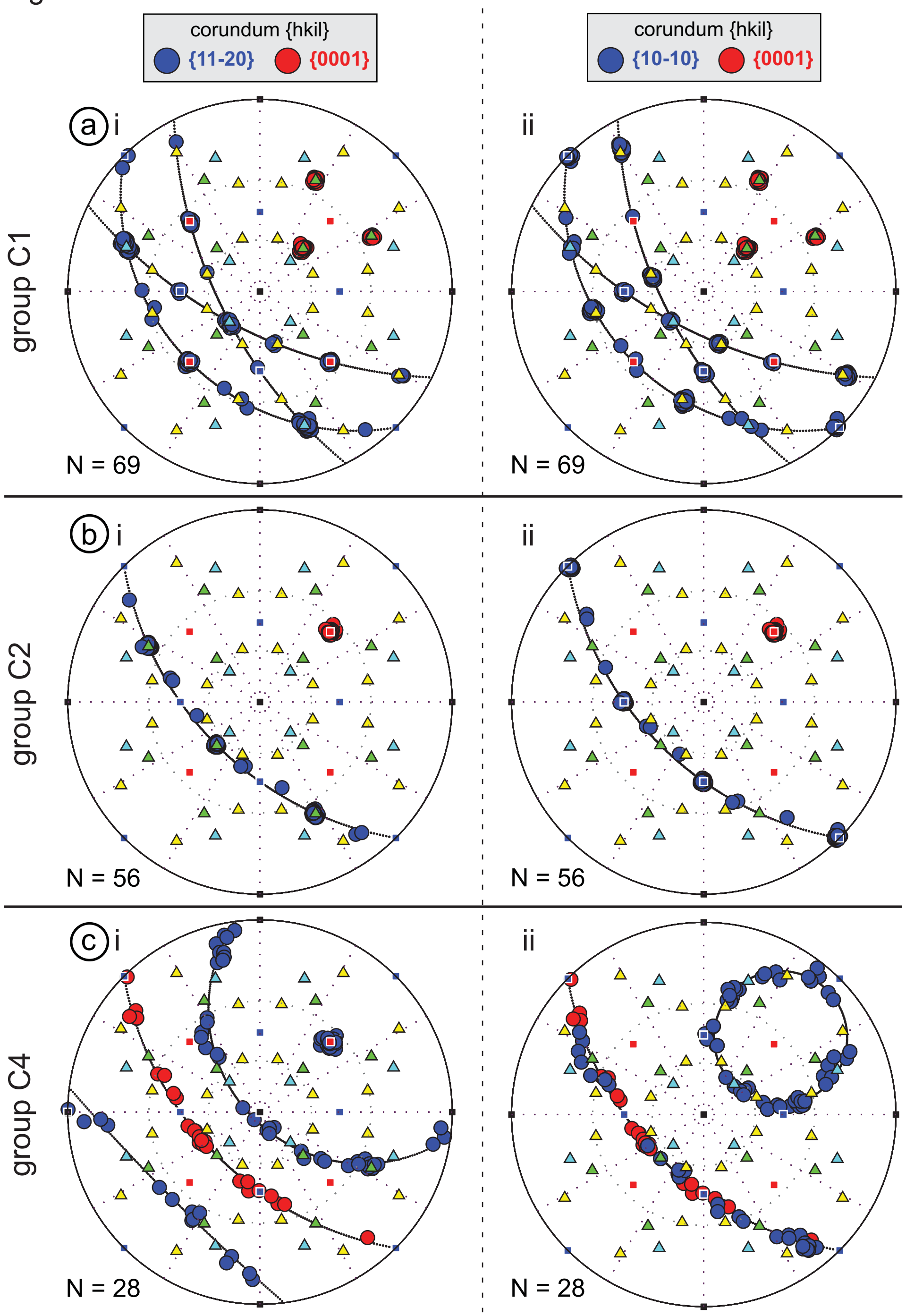
corundum {hkil}
{11-20} {0001}
corundum {hkil}
{10-10} {0001}
a i
ii
group C1
N = 69
N = 69
b i
ii
group C2
N = 56
N = 56
c i
ii
group C4
N = 28
N = 28

Figure 7

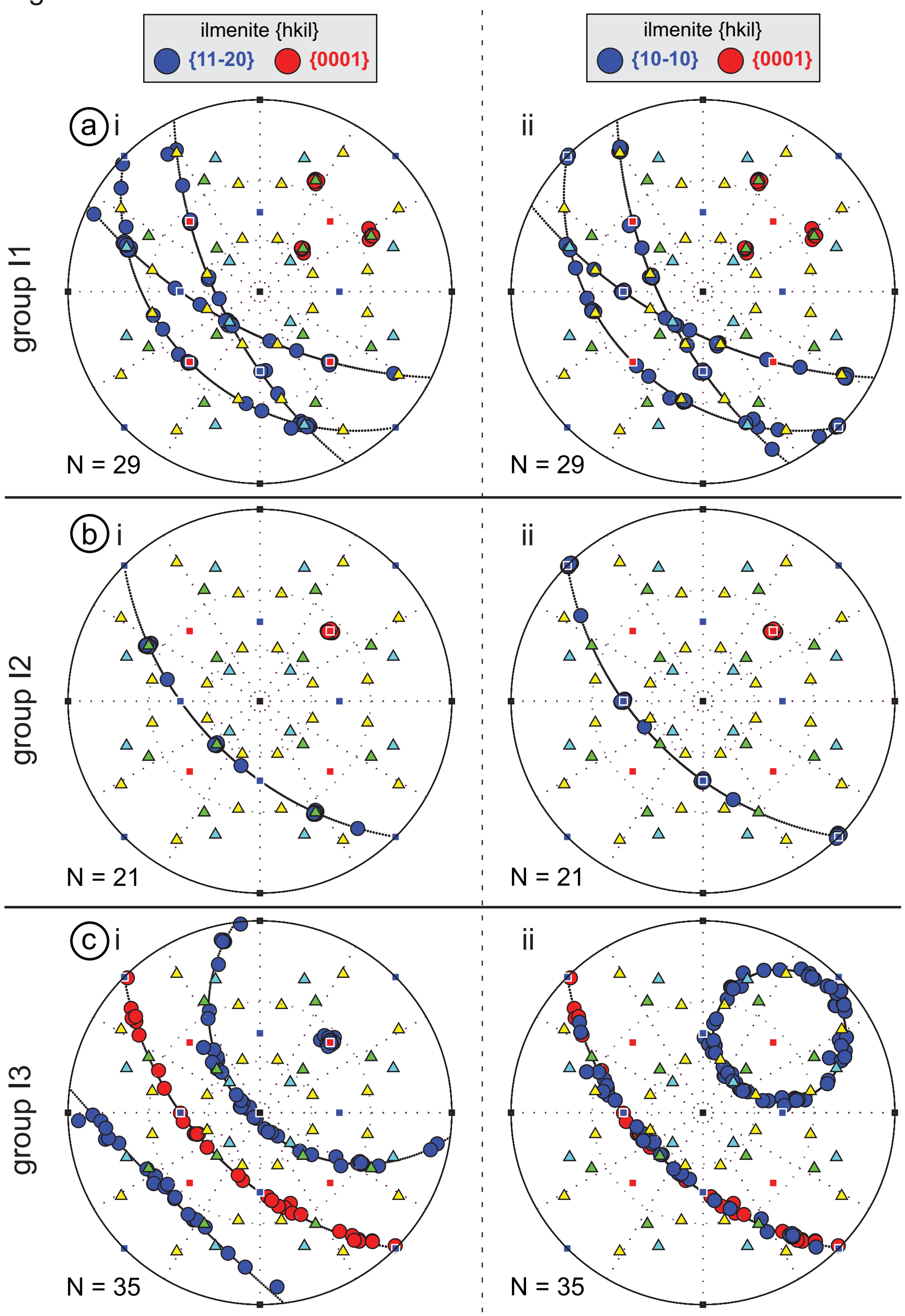
ilmenite {hkil}
{11-20}
{0001}
ilmenite {hkil}
{10-10}
{0001}
a
i
ii
b
i
ii
c
i
ii
group I1
group I2
group I3
N = 29
N = 29
N = 21
N = 21
N = 35
N = 35

Figure 8

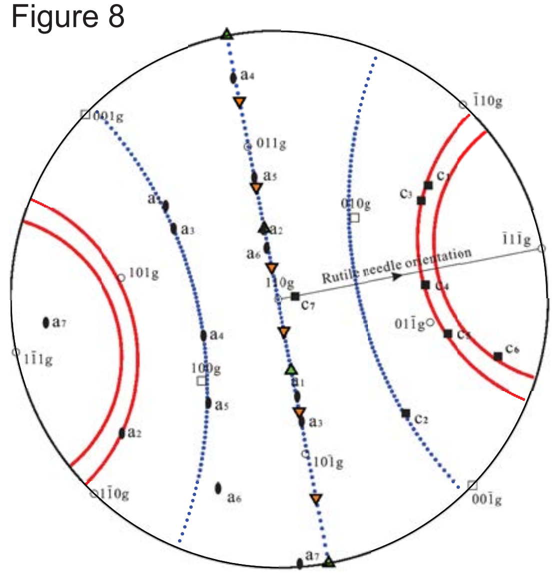
001g
011g
1̄10g
010g
1̄11̄g
101g
110g
Rutile needle orientation
01̄1̄g
11̄1g
100g
101̄g
11̄0g
001̄g
a1
a2
a3
a4
a5
a6
a7
c1
c2
c3
c4
c5
c6
c7